A Novel Segment-switching Strategy with the Current Transient Overshoot Suppression for Segmented Long-stator Linear Motor

Yanfei Li, Zixin Li, *Senior Member, IEEE*, Hang Zhang, Fei Xu, *Member, IEEE*,
Cong Zhao, *Member, IEEE*, Fanqiang Gao, *Member, IEEE*, and Yaohua Li

***Abstract*—The segmented power supply scheme for long-stator linear motor facilitates reducing power capacity and achieving a high power factor. However, the segment-switching process leads to overcurrent under high-speed conditions. This paper proposes a novel segment-switching strategy based on the time-optimal control theory. It employs time-optimal feedforward voltage and planned current trajectory during the switching transient process. Thus, it ensures rapid disconnection of the exiting segment and rapid establishment of the current in the incoming segment, while suppressing transient current overshoot. The mathematical model of the long-stator linear motor is established in the process of segment-switching. It derives the minimum times required to force the exiting segment current to zero and to establish the incoming segment current to the reference value by time-optimal control theory. Furthermore, the time-optimal voltages and current trajectories are calculated. The time-optimal current trajectories are used as the reference command for the current loop. The time-optimal feedforward voltages are introduced into the current loop control. Hence, it achieves rapid disconnection of the exiting segment and fast, accurate establishment of the incoming segment current. Experimental and simulation results collectively validate the effectiveness of the proposed segment-switching strategy.**

***Index Terms*—Long-stator linear motor**, **Segmented power supply**, **Segment switching**, **Longitudinal static end-effect**, **Time-optimal control**.

I. INTRODUCTION

LONG-STATOR linear motors (LSLM) offer advantages such as a simple mover structure [1] and reduced longitudinal dynamic end-effect [2], demonstrating broad application prospects in fields including high-speed rail transit [3], electromagnetic catapult [4]-[5], and electromagnetic propulsion high-speed ground test facilities [6]. A typical drive system for a long-stator linear motor is illustrated in Fig. 1. The long stator is generally designed in a modular fashion [7], assembled from multiple stator segments. Each stator segment is fed by a converter via an independent switch device. The system operates under a segmented power supply scheme: A switch is turned on only when its corresponding stator segment couples with the mover and remains off otherwise. This operating mode allows the converter to supply power only to a few stator segments coupled with the mover, thereby reducing the required converter capacity and improving system efficiency.

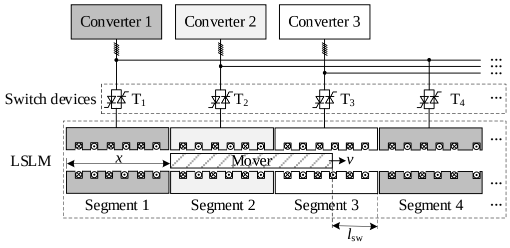

Fig. 1. Schematic of the segmented power supply principle in a long-stator linear motor.

However, the segmented power supply scheme introduces an additional control task: To generate stable thrust, the stator segments covering the mover must produce a continuous traveling magnetic field. The key to achieving this lies in the timely establishment of a continuously distributed spatial magnetic field during the segment-switching process. This necessitates the design of a corresponding segment-switching control strategy, which must disconnect the exiting segment from the converter while rapidly and precisely establishing a synchronized current in the incoming segment. Taking stator Segment 1 and Segment 4, both supplied by Converter 1 in Fig. 1, as an example: When the mover couples with Segment 1, Switches T_1, T_2, and T_3 are turned on. The three converters supply currents of identical amplitude and phase to Segments 1, 2, and 3, respectively, thereby forming a continuous traveling magnetic field over the region covered by the mover. After the mover leaves Segment 1, Converter 1 stops supplying power to it (Switch T_1 is turned off, thus disconnecting Segment 1). Simultaneously, to extend the continuous traveling magnetic field into the region of

Manuscript received March 31, 2026; revised April 14, 2026; accepted April 28, 2026. Date of publication June 25, 2026. Date of current version May 20, 2026.

This work was supported in part by the CAS Project for Young Scientists in Basic Research under Grant YSBR-045 and the Strategic Priority Research Program of Chinese Academy of Sciences under Grant XDB1330000.

Yanfei Li, Zixin Li, Hang Zhang, Fei Xu, Cong Zhao, Fanqiang Gao, and Yaohua Li are with the State Key Laboratory of High Density Electromagnetic Power and Systems, Institute of Electrical Engineering, Chinese Academy of Sciences, Beijing 100190, China, and also with the Univercity of Chinese Academy of Sciences, Beijing 100049, China (e-mail: liyf@mail.iee.ac.cn; lzx@mail.iee.ac.cn; zhanghang215@mail.iee.ac.cn; xufei@mail.iee.ac.cn; zhaocong@mail.iee.ac.cn; gaofanqiang@mail.iee.ac.cn; yhli@ mail.iee.ac.cn).

(*Corresponding Author: Cong Zhao*)

Digital Object Identifier 10.30941/CESTEMS.2026.00017

Segment 4 in advance, Converter 1 must precisely regulate the current in Segment 4 to a state synchronized with that of the adjacent segment (Segment 2 or 3) before the mover enters it (i.e., within the mover's travel distance l_{sw} shown in Fig. 1).

In high-speed driving scenarios, segment switching faces tight temporal constraints: Since the switching distance l_{sw} is typically fixed, the allowable time window for switching shortens as the speed increases. This challenge is particularly pronounced in short-duration, high-acceleration systems such as high-speed electromagnetic propulsion, where the payload must be accelerated to near the speed of sound within a few seconds, requiring the segment switching process to be completed within milliseconds. If the exiting segment cannot be reliably disconnected and the current in the incoming segment is rapidly and precisely synchronized within this narrow window, the continuity of the traveling magnetic field will be disrupted, leading to thrust fluctuations. In mild cases, this results in degraded acceleration performance; in severe cases, it can cause a loss of thrust control that may ultimately lead to a serious accident.

To ensure stable operation at high speeds, rapid segment switching capability is essential. The conventional switching method [8] is as follows: When the switching instant arrives, the switch device of the incoming segment is turned on immediately, while a turn-off command is simultaneously issued to the switch device of the exiting segment. Due to the high voltage and large current involved, short-duration high-acceleration systems commonly employ bidirectional thyristors (TRIACs) as switching devices. However, limited by the zero-crossing turn-off characteristic of thyristors, the above switching process is inherently accompanied by a transient condition where two stator segments are connected in parallel [8]. This parallel state reduces the equivalent load impedance by half, which can easily induce significant current overshoot and thereby threaten the safe operation of the power devices in the converter.

To address the current overshoot problem inherent in conventional switching methods, a series of improvement studies have been conducted, focusing on aspects such as supply topology, switching phase angle, switching sequence, and switching voltage. References [9]-[12] proposed a phase-by-phase switching strategy based on current zero-crossing detection. Their core principle is to modify the supply topology to establish independent current paths for each phase winding of the stator segments. This enables the exiting segment to be disconnected phase-by-phase as its current crosses zero, while simultaneously energizing the corresponding phase winding of the incoming segment, thereby avoiding the parallel connection of same-phase windings from two different segments. Representative solutions include configuring the stator winding in a delta connection [9], adding an inter-segment busbar [10]-[11], and connecting the neutral points of the windings from two stator segments [12]. The limitations of these strategies are the need for additional cables, which increases cost, and their reliance on precise detection of the current zero-crossing instant. Under high-speed operating conditions, the high output current frequency of the converter results in very short intervals between consecutive zero-crossings, making accurate detection challenging. Reference [13] suppressed current overshoot by optimizing the switching phase angle, yet the overshoot magnitude could still reach up to 50% even after optimization. Reference [14] investigated the influence of the switching sequence on the switching current and proposed a symmetrical switching method characterized by sequential turn-off and reverse-sequential turn-on; however, this method also depends on current zero-crossing detection. Reference [15] introduced a switching strategy that reduces the input voltage by half during the transition. Reference [16] calculates the switching voltage based on a planned current trajectory. However, both methods were derived under symmetrical inductance assumptions and are not suitable for linear motors with significant longitudinal static end-effect [17].

This paper proposes a fast and smooth segment-switching strategy based on time-optimal control theory. A mathematical model of a segmented long-stator linear motor in the segment-switching process, considering longitudinal static end-effect, is established. Based on time-optimal control theory, the time-optimal voltages required for disconnecting the exiting segment and establishing the current in the incoming segment, as well as the corresponding optimal current trajectories, are derived separately. The minimum required switching time is also quantitatively analyzed. Building on this, the time-optimal current trajectories are used as the reference command. Through the weighted fusion of the time-optimal voltage feedforward term and the current closed-loop feedback term, rapid decay of the exiting-segment current and accurate establishment of the incoming-segment current are achieved. The paper is organized as follows. Section II develops the mathematical model of the linear motor in the segment-switching process. Building on this model, section III analyzes the switching process using time-optimal control theory, and based on the analysis results, an improved segment-switching strategy is proposed in section IV. The effectiveness of the strategy is then validated experimentally in section V. Finally, section VI concludes the paper.

II. MATHEMATICAL MODEL OF SEGMENTED POWER SUPPLY LINEAR MOTOR IN THE SWITCHING PROCESS

A. *Model in the Original Six-dimensional Space*

To ensure smooth thrust, the segment-switching process is scheduled to occur when both segments involved are not coupled with the mover. Taking the switching between Segment 1 and Segment 4 in Fig. 1 as an example, this process takes place during the interval after the mover has completely left Segment 1 and before it enters Segment 4. Throughout this interval, thrust is provided solely by Segment 2 and Segment 3, which remain coupled with the mover, thereby decoupling the switching process from thrust production. Consequently, when establishing the mathematical model of the segment-switching process, it is sufficient to consider only the no-load condition of the stator segments.

Fig. 2 shows a schematic diagram of the stator segment operating under no-load conditions. To reduce the per-phase current requirement and enhance system fault tolerance [18], a dual three-phase (dual-Y shift 30°) winding configuration is adopted for the stator segment. The two sets of three-phase windings, UVW and XYZ, each have an independent neutral point, denoted as o_1 and o_2, respectively. Each phase winding is supplied by the converter via a TRIAC.

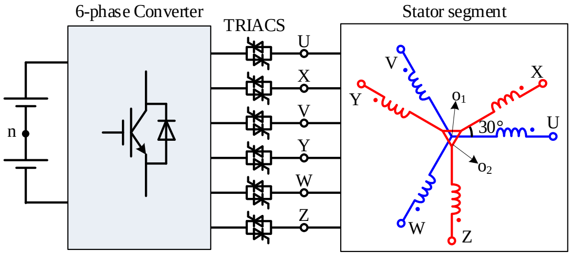

Fig. 2. Schematic diagram of the stator segment operating under no-load conditions.

Segmented long-stator linear induction motors exhibit a pronounced longitudinal static end-effect, i.e., in addition to the traveling magnetic field, a pulsating offset magnetic field component exists in the air-gap flux of the energized stator segment [19]-[20]. The six-phase inductance matrix of the stator segment $\boldsymbol{L}_{\mathrm{s}}$ can be decomposed into a symmetric part $\boldsymbol{L}_{\mathrm{s(sy)}}$ and an asymmetric part $\boldsymbol{L}_{\mathrm{s(asy)}}$ as:

$$\boldsymbol{L}_{\mathrm{s}} = \boldsymbol{L}_{\mathrm{s(sy)}} + \boldsymbol{L}_{\mathrm{s(asy)}} \tag{1}$$

In the symmetric inductance matrix, mutual inductances between two phases with the same spatial phase difference are identical. Let M_{30}, M_{60}, M_{90}, M_{120}, and M_{150} denote the symmetric mutual inductances for phase differences of 30°, 60°, 90°, 120°, and 150°, respectively. After arrangement, the symmetric inductance matrix $\boldsymbol{L}_{\mathrm{s(sy)}}$ can be expressed as:

$$\boldsymbol{L}_{\mathrm{s(sy)}} = \begin{bmatrix} L_0 & M_{30} & M_{120} & M_{150} & M_{120} & M_{90} \\ M_{30} & L_0 & M_{90} & M_{120} & M_{150} & M_{120} \\ M_{120} & M_{90} & L_0 & M_{30} & M_{120} & M_{150} \\ M_{150} & M_{120} & M_{30} & L_0 & M_{90} & M_{120} \\ M_{120} & M_{150} & M_{120} & M_{90} & L_0 & M_{30} \\ M_{90} & M_{120} & M_{150} & M_{120} & M_{30} & L_0 \end{bmatrix} \tag{2}$$

where L_0 is the self-inductance in the symmetric matrix. Furthermore, the relations $M_{30} = -M_{150}$ and $M_{90} = 0$ hold.

The asymmetric inductance matrix $\boldsymbol{L}_{\mathrm{s(asy)}}$ describes the inductance characteristics arising from the pulsating offset magnetic field in segmented long-stator linear motors [21], and takes (3):

$$\boldsymbol{L}_{\mathrm{s(asy)}} = L_{\mathrm{dc}} \begin{bmatrix} 1 & 1 & 1 & 1 & -1 & -1 \\ 1 & 1 & 1 & 1 & -1 & -1 \\ 1 & 1 & 1 & 1 & -1 & -1 \\ 1 & 1 & 1 & 1 & -1 & -1 \\ -1 & -1 & -1 & -1 & 1 & 1 \\ -1 & -1 & -1 & -1 & 1 & 1 \end{bmatrix} \tag{3}$$

where L_{dc} denotes the absolute value of the asymmetric mutual inductance.

Furthermore, due to the longitudinal static end-effect, mutual inductance exists between a stator segment and its adjacent segments on both sides. Fig. 3 shows a schematic diagram of the pulsating offset magnetic field distribution generated by a single-phase winding [21]. The figure illustrates the pulsating offset magnetic field produced by a unit current flowing through a single-phase winding of stator segment Seg0. This field is symmetrically distributed on the left and right sides of the energized segment. Owing to the gaps between stator segments, the intensity of the pulsating offset magnetic field gradually decays with increasing distance from the energized segment. Let the intensity of the pulsating offset magnetic field in the air gap of Seg0 be B_{dc0}, the intensities in the air gaps of SegL1 and SegR1 both be $-k_1B_{\mathrm{dc0}}$, and those in the air gaps of SegL2 and SegR2 be $-k_2B_{\mathrm{dc0}}$, where k_1 and k_2 are proportionality coefficients satisfying $0 < k_1, k_2 < 1$. Accordingly, the mutual inductance matrix $\boldsymbol{M}_1$ between Seg0 and SegL1 (or SegR1), and the mutual inductance matrix $\boldsymbol{M}_2$ between Seg0 and SegL2 (or SegR2), are given as (4):

$$\boldsymbol{M}_1 = -k_1\boldsymbol{L}_{\mathrm{s(asy)}}, \boldsymbol{M}_2 = -k_2\boldsymbol{L}_{\mathrm{s(asy)}} \tag{4}$$

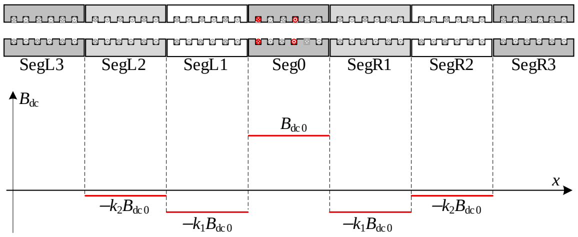

Fig. 3. Schematic diagram of the pulsating offset magnetic field distribution generated by a single-phase winding.

In this paper, it is assumed that the pulsating offset magnetic field decays to zero after passing through two stator segments. Then, according to the flux continuity theorem, we have:

$$k_1 + k_2 = 0.5 \tag{5}$$

The voltage equation of the stator segment Seg0 in the original six-dimensional space is:

$$\begin{aligned} \boldsymbol{u}_{\mathrm{s}} - \boldsymbol{u}_{\mathrm{on}} = {} & R_{\mathrm{s}}\boldsymbol{i}_{\mathrm{s}} + \boldsymbol{L}_{\mathrm{s}}p\boldsymbol{i}_{\mathrm{s}} - k_1\boldsymbol{L}_{\mathrm{s(asy)}}p\boldsymbol{i}_{\mathrm{sL1}} - k_1\boldsymbol{L}_{\mathrm{s(asy)}}p\boldsymbol{i}_{\mathrm{sR1}} - \\ & k_2\boldsymbol{L}_{\mathrm{s(asy)}}p\boldsymbol{i}_{\mathrm{sL2}} - k_2\boldsymbol{L}_{\mathrm{s(asy)}}p\boldsymbol{i}_{\mathrm{sR2}} \end{aligned} \tag{6}$$

where p is the time differential operator, R_{s} is the phase resistance of the stator segment. $\boldsymbol{u}_{\mathrm{s}}$ denotes the six-phase voltage output from the converter, $\boldsymbol{u}_{\mathrm{on}}$ represents the voltage from each neutral point to point n in Fig. 2, and $\boldsymbol{i}_{\mathrm{s}}$, $\boldsymbol{i}_{\mathrm{sL1}}$, $\boldsymbol{i}_{\mathrm{sR1}}$, $\boldsymbol{i}_{\mathrm{sL2}}$, and $\boldsymbol{i}_{\mathrm{sR2}}$ are the currents of the Seg0, SegL1, SegR1, SegL2, and SegR2, respectively. The specific forms of $\boldsymbol{u}_{\mathrm{s}}$, $\boldsymbol{u}_{\mathrm{on}}$, and $\boldsymbol{i}_{\mathrm{s}}$ are in (7):

$$\boldsymbol{u}_{\mathrm{s}} = \begin{bmatrix} u_{\mathrm{Un}} \\ u_{\mathrm{Xn}} \\ u_{\mathrm{Vn}} \\ u_{\mathrm{Yn}} \\ u_{\mathrm{Wn}} \\ u_{\mathrm{Zn}} \end{bmatrix}, \boldsymbol{u}_{\mathrm{on}} = \begin{bmatrix} u_{\mathrm{o1n}} \\ u_{\mathrm{o2n}} \\ u_{\mathrm{o1n}} \\ u_{\mathrm{o2n}} \\ u_{\mathrm{o1n}} \\ u_{\mathrm{o2n}} \end{bmatrix}, \boldsymbol{i}_{\mathrm{s}} = \begin{bmatrix} i_{\mathrm{U}} \\ i_{\mathrm{X}} \\ i_{\mathrm{V}} \\ i_{\mathrm{Y}} \\ i_{\mathrm{W}} \\ i_{\mathrm{Z}} \end{bmatrix} \tag{7}$$

B. *Vector Space Decomposition (VSD) Model*

For dual three-phase rotating machines, the VSD transformation [22] is typically employed to simplify the original six-phase model. Through this transformation, the six-phase voltage and current vectors are mapped into three decoupled subspaces: the αβ subspace, associated with electromechanical energy conversion; the z_1z_2 subspace, related to harmonic components; and the 0_10_2 subspace, which, due to the star connection of the windings, carries no zero-sequence current and is therefore usually negligible.

However, influenced by the asymmetric part of the inductance matrix, $\boldsymbol{L}_{\mathrm{s(asy)}}$, severe coupling appears between the αβ and z_1z_2 subspaces after the conventional VSD transformation. Therefore, based on the special structure of $\boldsymbol{L}_{\mathrm{s(asy)}}$, this paper analyzes the transformed result of using the conventional VSD transformation matrix and derives an improved VSD transformation matrix $\boldsymbol{T}_{\mathrm{VSD(imp)}}$, as given in (8), which can simplify the transformed inductance matrix. The detailed derivation is presented in Appendix I.

$$\boldsymbol{T}_{\mathrm{VSD(imp)}}^{\mathrm{T}}=\frac{1}{3}\begin{bmatrix}\cos(\theta_\alpha) & -\sin(\theta_\alpha) & \cos(\theta_\alpha) & \sin(\theta_\alpha)\\ \cos\left(\theta_\alpha-\frac{\pi}{6}\right) & -\sin\left(\theta_\alpha-\frac{\pi}{6}\right) & -\cos\left(\theta_\alpha-\frac{\pi}{6}\right) & -\sin\left(\theta_\alpha-\frac{\pi}{6}\right)\\ \cos\left(\theta_\alpha-\frac{2\pi}{3}\right) & -\sin\left(\theta_\alpha-\frac{2\pi}{3}\right) & \cos\left(\theta_\alpha-\frac{2\pi}{3}\right) & \sin\left(\theta_\alpha-\frac{2\pi}{3}\right)\\ \cos\left(\theta_\alpha-\frac{5\pi}{6}\right) & -\sin\left(\theta_\alpha-\frac{5\pi}{6}\right) & -\cos\left(\theta_\alpha-\frac{5\pi}{6}\right) & -\sin\left(\theta_\alpha-\frac{5\pi}{6}\right)\\ \cos\left(\theta_\alpha+\frac{2\pi}{3}\right) & -\sin\left(\theta_\alpha+\frac{2\pi}{3}\right) & \cos\left(\theta_\alpha+\frac{2\pi}{3}\right) & \sin\left(\theta_\alpha+\frac{2\pi}{3}\right)\\ \cos\left(\theta_\alpha+\frac{\pi}{2}\right) & -\sin\left(\theta_\alpha+\frac{\pi}{2}\right) & -\cos\left(\theta_\alpha+\frac{\pi}{2}\right) & -\sin\left(\theta_\alpha+\frac{\pi}{2}\right)\end{bmatrix} \tag{8}$$

where $\theta_\alpha = 5\pi/12$. By adopting the improved VSD transformation, the voltage equation given in (6) becomes:

$$\begin{aligned}\boldsymbol{u}_{\alpha\beta z1z2}=&R_s\boldsymbol{i}_{\alpha\beta z1z2}+\boldsymbol{L}_{\alpha\beta z1z2}p\boldsymbol{i}_{\alpha\beta z1z2}-\\ &k_1\boldsymbol{M}_{\mathrm{dc}}p\boldsymbol{i}_{\mathrm{L1\_}\alpha\beta z1z2}-k_1\boldsymbol{M}_{\mathrm{dc}}p\boldsymbol{i}_{\mathrm{R1\_}\alpha\beta z1z2}-\\ &k_2\boldsymbol{M}_{\mathrm{dc}}p\boldsymbol{i}_{\mathrm{L2\_}\alpha\beta z1z2}-k_2\boldsymbol{M}_{\mathrm{dc}}p\boldsymbol{i}_{\mathrm{R2\_}\alpha\beta z1z2}\end{aligned} \tag{9}$$

where, $\boldsymbol{u}_{\alpha\beta z1z2}$, $\boldsymbol{i}_{\alpha\beta z1z2}$, and $\boldsymbol{L}_{\alpha\beta z1z2}$ denote the voltage vector, current vector, and inductance matrix of Seg0 in the $\alpha\beta z_1z_2$ space, respectively, expressed as:

$$\boldsymbol{u}_{\alpha\beta z1z2}=\begin{bmatrix}u_\alpha\\u_\beta\\u_{z1}\\u_{z2}\end{bmatrix},\boldsymbol{i}_{\alpha\beta z1z2}=\begin{bmatrix}i_\alpha\\i_\beta\\i_{z1}\\i_{z2}\end{bmatrix},\boldsymbol{L}_{\alpha\beta z1z2}=\begin{bmatrix}L_\alpha & 0 & 0 & M_{\alpha z2}\\0 & L_\beta & 0 & 0\\0 & 0 & L_{z1} & 0\\M_{\alpha z2} & 0 & 0 & L_{z2}\end{bmatrix} \tag{10}$$

The elements of $\boldsymbol{L}_{\alpha\beta z1z2}$: L_α, L_β, L_{z1}, L_{z2}, and $M_{\alpha z2}$ are as (11):

$$\begin{cases}L_\alpha=L_0-M_{120}+\sqrt{3}/2\left(M_{30}-M_{150}\right)+4\left(2+\sqrt{3}\right)/3L_{\mathrm{dc}}\\ L_\beta=L_0-M_{120}+\sqrt{3}/2\left(M_{30}-M_{150}\right)\\ L_{z1}=L_0-M_{120}+\sqrt{3}/2\left(M_{150}-M_{30}\right)\\ L_{z2}=L_0-M_{120}+\sqrt{3}/2\left(M_{150}-M_{30}\right)+4\left(2-\sqrt{3}\right)/3L_{\mathrm{dc}}\\ M_{\alpha z2}=\frac{4}{3}L_{\mathrm{dc}}\end{cases} \tag{11}$$

And $\boldsymbol{i}_{\mathrm{L1\_}\alpha\beta z1z2}$, $\boldsymbol{i}_{\mathrm{R1\_}\alpha\beta z1z2}$, $\boldsymbol{i}_{\mathrm{L2\_}\alpha\beta z1z2}$, and $\boldsymbol{i}_{\mathrm{R2\_}\alpha\beta z1z2}$ represent the current vector of SegL1, SegR1, SegL2, and SegR2 in the $\alpha\beta z_1z_2$ space, respectively. $\boldsymbol{M}_{\mathrm{dc}}$ is the result obtained by applying the improved VSD transformation to $\boldsymbol{L}_{\mathrm{s(asy)}}$, and its specific form is given as (12): It can be observed that in the inductance matrix $\boldsymbol{L}_{\alpha\beta z1z2}$ and $\boldsymbol{M}_{\mathrm{dc}}$ obtained via the improved VSD transformation, mutual coupling exists only between the α and z_2 axes. This achieves an approximate decoupling among the four variables in the $\alpha\beta z_1z_2$ space, which facilitates: simplified analysis and control of the system. The following section analyzes the segment-switching process using this simplified model.

$$\boldsymbol{M}_{\mathrm{dc}}=\frac{4}{3}L_{\mathrm{dc}}\begin{bmatrix}2+\sqrt{3} & 0 & 0 & 1\\0 & 0 & 0 & 0\\0 & 0 & 0 & 0\\1 & 0 & 0 & 2-\sqrt{3}\end{bmatrix} \tag{12}$$

III. ANALYSIS OF TIME-OPTIMAL CONTROL FOR SEGMENT SWITCHING

Due to the zero-crossing turn-off characteristic of thyristors, a parallel transient condition between the exiting and incoming segments occurs during conventional segment switching, leading to a sudden change in load impedance. This not only imposes extremely high demands on the controller's dynamic response and easily triggers overcurrent faults, but the delayed turn-off of the exiting segment's current also interferes with the regulation of the incoming segment's current. To address these issues, the two processes can be completely separated in time sequence: after the exiting segment current is fully disconnected, the current establishment of the incoming segment is initiated, thereby achieving dual decoupling in both physical connection and current control. To prevent the time separation from increasing the overall switching duration, this section analyzes the two processes separately based on time-optimal control theory, aiming to compress their respective completion times and achieve fast switching without current impact.

To facilitate the analysis, (9) is first simplified according to the operating characteristics of the segment-switching process. During the segment-switching transient, only one side of the stator segment has energized adjacent segments (for example, in Fig. 1, when switching from Segment 1 to Segment 4, only Segments 2 and 3 on the left side of Segment 4 carry current), and the currents in the adjacent segments can track their references well. Based on the above characteristics, (9) can be simplified as:

$$\begin{aligned}\boldsymbol{u}_{\alpha\beta z1z2} = &R_{\mathrm{s}}\boldsymbol{i}_{\alpha\beta z1z2} + \boldsymbol{L}_{\alpha\beta z1z2}p\boldsymbol{i}_{\alpha\beta z1z2} - \\ &\left(k_1+k_2\right)\boldsymbol{M}_{\mathrm{dc}}p\boldsymbol{i}_{\mathrm{ref\_}\alpha\beta z1z2}\end{aligned} \tag{13}$$

where $\boldsymbol{i}_{\mathrm{ref\_}\alpha\beta z1z2} = [i_{\mathrm{ref}\alpha} \quad i_{\mathrm{ref}\beta} \quad 0 \quad 0]^{\mathrm{T}}$, combining (5) and (12) yields:

$$\boldsymbol{u}_{\mathrm{M}} = -\left(k_1+k_2\right)\boldsymbol{M}_{\mathrm{dc}}p\boldsymbol{i}_{\mathrm{ref\_}\alpha\beta z1z2} = \frac{4+2\sqrt{3}}{3}L_{\mathrm{dc}}p\begin{bmatrix} i_{\mathrm{ref}\alpha} \\ 0 \\ 0 \\ 0 \end{bmatrix} \tag{14}$$

where, $\boldsymbol{u}_{\mathrm{M}}$ represents the adjacent-segment mutual inductance voltage. Furthermore, since $pi_{\mathrm{ref}\alpha} = -\omega_{\mathrm{e}}i_{\mathrm{ref}\beta}$, the $\boldsymbol{u}_{\mathrm{M}}$ can be expressed as:

$$\boldsymbol{u}_{\mathrm{M}} = \frac{4+2\sqrt{3}}{3}L_{\mathrm{dc}}\left[\omega_{\mathrm{e}}i_{\mathrm{ref}\beta} \quad 0 \quad 0 \quad 0\right]^{\mathrm{T}} \tag{15}$$

where ω_{e} is the stator synchronous angular frequency. On this basis, by canceling the stator resistance voltage drop and the adjacent-segment mutual inductance voltage in (13) via feedforward compensation, (13) can be reduced to:

$$p\boldsymbol{i}_{\alpha\beta z1z2} = \boldsymbol{L}_{\alpha\beta z1z2}^{-1}\boldsymbol{u}_{\alpha\beta z1z2} \tag{16}$$

Considering the practical constraint that the magnitude of the voltage vector is limited in actual systems:

$$\left\|\boldsymbol{u}_{\alpha\beta z1z2}\right\| = \sqrt{u_{\alpha}^2 + u_{\beta}^2 + u_{z1}^2 + u_{z2}^2} \le U_{\mathrm{m}} \tag{17}$$

where ||.|| denotes the magnitude of a vector. For the linear time-invariant system described by (16) (neglecting magnetic saturation), the Hamiltonian function [23]-[24] can be written as:

$$H = 1 + \boldsymbol{u}_{\alpha\beta z1z2}^{\mathrm{T}}\left(t\right)\left(\boldsymbol{L}_{\alpha\beta z1z2}^{-1}\right)^{\mathrm{T}}\boldsymbol{P}\left(t\right) \tag{18}$$

where $\boldsymbol{P}(t)$ is the costate variable:

$$\boldsymbol{P}\left(t\right) = \left[p_{\alpha}\left(t\right) \quad p_{\beta}\left(t\right) \quad p_{z1}\left(t\right) \quad p_{z2}\left(t\right)\right]^{\mathrm{T}} \tag{19}$$

and its time derivative satisfies:

$$\begin{bmatrix} \mathrm{d}p_{\alpha}/\mathrm{d}t \\ \mathrm{d}p_{\beta}/\mathrm{d}t \\ \mathrm{d}p_{z1}/\mathrm{d}t \\ \mathrm{d}p_{z2}/\mathrm{d}t \end{bmatrix} = -\begin{bmatrix} \partial H/\partial i_{\alpha}\left(t\right) \\ \partial H/\partial i_{\beta}\left(t\right) \\ \partial H/\partial i_{z1}\left(t\right) \\ \partial H/\partial i_{z2}\left(t\right) \end{bmatrix} = \begin{bmatrix} 0 \\ 0 \\ 0 \\ 0 \end{bmatrix} \tag{20}$$

Hence, the costate variable is constant and can be denoted as a fixed vector $\boldsymbol{P}_0$, i.e., $\boldsymbol{P}(t) = \boldsymbol{P}_0$.

According to the maximum principle, the time-optimal input voltage $\boldsymbol{u}_{\alpha\beta z1z2}^{*}(t)$ should minimize the Hamiltonian at every instant:

$$1 + \left(\boldsymbol{u}_{\alpha\beta z1z2}^{*}\left(t\right)\right)^{\mathrm{T}}\left(\boldsymbol{L}_{\alpha\beta z1z2}^{-1}\right)^{\mathrm{T}}\boldsymbol{P}_0 \le 1 + \boldsymbol{u}_{\alpha\beta z1z2}^{\mathrm{T}}\left(t\right)\left(\boldsymbol{L}_{\alpha\beta z1z2}^{-1}\right)^{\mathrm{T}}\boldsymbol{P}_0 \tag{21}$$

From the properties of the vector inner product, for (21) to hold, the direction of $\boldsymbol{u}_{\alpha\beta z1z2}^{*}(t)$ must be opposite to that of the vector $(\boldsymbol{L}_{\alpha\beta z1z2}^{-1})^{\mathrm{T}}\boldsymbol{P}_0$, and its magnitude should take the maximum value U_{m} [23]:

$$\boldsymbol{u}_{\alpha\beta z1z2}^{*}\left(t\right) = -\left(U_{\mathrm{m}} / \left\|\left(\boldsymbol{L}_{\alpha\beta z1z2}^{-1}\right)^{\mathrm{T}}\boldsymbol{P}_0\right\|\right)\left(\boldsymbol{L}_{\alpha\beta z1z2}^{-1}\right)^{\mathrm{T}}\boldsymbol{P}_0 \tag{22}$$

Consequently, the time-optimal voltage $\boldsymbol{u}_{\alpha\beta z1z2}^{*}(t)$ is a constant vector in the $\alpha\beta z_1z_2$ frame. Substituting it into (16) yields the evolution of the current vector $\boldsymbol{i}_{\alpha\beta z1z2}$ under time-optimal voltage:

$$\boldsymbol{i}_{\alpha\beta z1z2}\left(t\right) = \boldsymbol{i}_{\alpha\beta z1z2}\left(0\right) + \boldsymbol{L}_{\alpha\beta z1z2}^{-1}\boldsymbol{u}_{\alpha\beta z1z2}^{*}t \tag{23}$$

Assume that after the optimal time t^{*}, the current vector reaches the target value $\boldsymbol{i}_{\alpha\beta z1z2}^{\mathrm{goal}}$, i.e.:

$$\boldsymbol{i}_{\alpha\beta z1z2}\left(t^{*}\right) = \boldsymbol{i}_{\alpha\beta z1z2}^{\mathrm{goal}} \tag{24}$$

From (23), at time t^{*}, we have:

$$\boldsymbol{i}_{\alpha\beta z1z2}^{\mathrm{goal}} - \boldsymbol{i}_{\alpha\beta z1z2}\left(0\right) = \boldsymbol{L}_{\alpha\beta z1z2}^{-1}\boldsymbol{u}_{\alpha\beta z1z2}^{*}t^{*} \tag{25}$$

Solving for the optimal time gives:

$$t^{*} = \left\|\boldsymbol{L}_{\alpha\beta z1z2}\left(\boldsymbol{i}_{\alpha\beta z1z2}^{\mathrm{goal}} - \boldsymbol{i}_{\alpha\beta z1z2}\left(0\right)\right)\right\| / U_{\mathrm{m}} \tag{26}$$

Combining (23) and (25) yields the trajectory of the current vector $\boldsymbol{i}_{\alpha\beta z1z2}$:

$$\boldsymbol{i}_{\alpha\beta z1z2}\left(t\right) - \boldsymbol{i}_{\alpha\beta z1z2}\left(0\right) = \left(t/t^{*}\right)\left[\boldsymbol{i}_{\alpha\beta z1z2}^{\mathrm{goal}} - \boldsymbol{i}_{\alpha\beta z1z2}\left(0\right)\right] \tag{27}$$

Thus, the current $\boldsymbol{i}_{\alpha\beta z1z2}$ varies linearly with time along the straight line connecting its initial value to the target value under the time-optimal voltage.

Additionally, (25) provides an alternative expression for the time-optimal voltage vector:

$$\boldsymbol{u}_{\alpha\beta z1z2}^{*} = \frac{1}{t^{*}}\boldsymbol{L}_{\alpha\beta z1z2}\left[\boldsymbol{i}_{\alpha\beta z1z2}^{\mathrm{goal}} - \boldsymbol{i}_{\alpha\beta z1z2}\left(0\right)\right] \tag{28}$$

It is worth noting that while (22) gives the magnitude U_{m} of the time-optimal voltage, its direction depends on the costate vector $\boldsymbol{P}_0$, which is not straightforward to obtain. Equation (28), however, explicitly provides the direction of the time-optimal voltage. Therefore, combining (22) and (28), a practical expression for the time-optimal voltage vector is obtained:

$$\boldsymbol{u}_{\alpha\beta z1z2}^{*} = U_{\mathrm{m}}\frac{\boldsymbol{L}_{\alpha\beta z1z2}\left[\boldsymbol{i}_{\alpha\beta z1z2}^{\mathrm{goal}} - \boldsymbol{i}_{\alpha\beta z1z2}\left(0\right)\right]}{\left\|\boldsymbol{L}_{\alpha\beta z1z2}\left[\boldsymbol{i}_{\alpha\beta z1z2}^{\mathrm{goal}} - \boldsymbol{i}_{\alpha\beta z1z2}\left(0\right)\right]\right\|} \tag{29}$$

That is, the magnitude of the time-optimal voltage vector is U_{m}, and its direction coincides with that of the vector $\boldsymbol{L}_{\alpha\beta z1z2}[\boldsymbol{i}_{\alpha\beta z1z2}^{\mathrm{goal}} - \boldsymbol{i}_{\alpha\beta z1z2}(0)]$.

Based on the above analytical results, the disconnection process of the exiting segment and the current-establishment process of the incoming segment are discussed separately below.

A. *Process of Disconnecting the Exiting Segment*

Based on the zero-crossing turn-off characteristic of thyristors, to rapidly disconnect the exiting segment, its six-phase currents must be reduced from their initial values to zero as quickly as possible. Denoting the current vector of the exiting segment in the αβz₁z₂ frame as $\boldsymbol{i}_{\alpha\beta\mathrm{z1z2(off)}}$, its target value, $\boldsymbol{i}^{\mathrm{goal}}_{\alpha\beta\mathrm{z1z2(off)}}$, is:

$$\boldsymbol{i}^{\mathrm{goal}}_{\alpha\beta\mathrm{z1z2(off)}} = \left(0,0,0,0\right)^{\mathrm{T}} \tag{30}$$

From (26) and (30), the minimum disconnection time for the exiting segment, t^*_{off}, is obtained as:

$$t^*_{\mathrm{off}} = \left\| \boldsymbol{L}_{\alpha\beta\mathrm{z1z2}} \boldsymbol{i}_{\alpha\beta\mathrm{z1z2(off)}}\left(0\right) \right\| / U_{\mathrm{m}} \tag{31}$$

where $\boldsymbol{i}_{\alpha\beta\mathrm{z1z2(off)}}(0)$ is the initial current of the exiting segment at the start of the segment-switching process.

Combining (29) with (30) yields the time-optimal voltage vector for the disconnection process, $\boldsymbol{u}^*_{\alpha\beta\mathrm{z1z2(off)}}$:

$$\boldsymbol{u}^*_{\alpha\beta\mathrm{z1z2(off)}} = -U_{\mathrm{m}} \frac{\boldsymbol{L}_{\alpha\beta\mathrm{z1z2}} \boldsymbol{i}_{\alpha\beta\mathrm{z1z2(off)}}\left(0\right)}{\left\| \boldsymbol{L}_{\alpha\beta\mathrm{z1z2}} \boldsymbol{i}_{\alpha\beta\mathrm{z1z2(off)}}\left(0\right) \right\|} \tag{32}$$

Equation (26) shows that $\boldsymbol{u}^*_{\alpha\beta\mathrm{z1z2(off)}}$ is a constant vector with magnitude U_{m} and direction opposite to that of $\boldsymbol{L}_{\alpha\beta\mathrm{z1z2}} \boldsymbol{i}_{\alpha\beta\mathrm{z1z2(off)}}(0)$.

Combining (27) with (30) gives the fastest-descending trajectory of the exiting-segment current:

$$\boldsymbol{i}_{\alpha\beta\mathrm{z1z2(off)}}\left(t\right) = \left(1 - t/t^*_{\mathrm{off}}\right) \boldsymbol{i}_{\alpha\beta\mathrm{z1z2(off)}}\left(0\right) \tag{33}$$

That is, in the αβz₁z₂ frame, the exiting-segment current linearly decreases from its initial value to zero.

B. Current Establishment Process of the Incoming Segment

During the establishment of the incoming segment, its six-phase currents must be raised from zero to synchronize with those of the mover-coupled segment as rapidly as possible. Denoting the current vector of the incoming segment as $\boldsymbol{i}_{\alpha\beta\mathrm{z1z2(on)}}$, its initial value is:

$$\boldsymbol{i}_{\alpha\beta\mathrm{z1z2(on)}}\left(0\right) = \left(0,0,0,0\right)^{\mathrm{T}} \tag{34}$$

From (26) and (34), the optimal (minimum) establishment time, t^*_{on}, is given by:

$$t^*_{\mathrm{on}} = \left\| \boldsymbol{L}_{\alpha\beta\mathrm{z1z2}} \boldsymbol{i}^{\mathrm{goal}}_{\alpha\beta\mathrm{z1z2(on)}} \right\| / U_{\mathrm{m}} \tag{35}$$

where $\boldsymbol{i}^{\mathrm{goal}}_{\alpha\beta\mathrm{z1z2(on)}}$ is the target current value for the incoming segment.

Using (29) and (34), the time-optimal voltage vector for the establishment process, $\boldsymbol{u}^*_{\alpha\beta\mathrm{z1z2(on)}}$, is derived as:

$$\boldsymbol{u}^*_{\alpha\beta\mathrm{z1z2(on)}} = U_{\mathrm{m}} \frac{\boldsymbol{L}_{\alpha\beta\mathrm{z1z2}} \boldsymbol{i}^{\mathrm{goal}}_{\alpha\beta\mathrm{z1z2(on)}}}{\left\| \boldsymbol{L}_{\alpha\beta\mathrm{z1z2}} \boldsymbol{i}^{\mathrm{goal}}_{\alpha\beta\mathrm{z1z2(on)}} \right\|} \tag{36}$$

Equation (30) indicates that $\boldsymbol{u}^*_{\alpha\beta\mathrm{z1z2(on)}}$ is a constant vector with magnitude U_{m} and direction identical to that of $\boldsymbol{L}_{\alpha\beta\mathrm{z1z2}} \boldsymbol{i}^{\mathrm{goal}}_{\alpha\beta\mathrm{z1z2(on)}}$.

From (27) and (34), the fastest-rising trajectory of the incoming-segment current is:

$$\boldsymbol{i}_{\alpha\beta\mathrm{z1z2(on)}}\left(t\right) = \left(t/t^*_{\mathrm{on}}\right) \boldsymbol{i}^{\mathrm{goal}}_{\alpha\beta\mathrm{z1z2(on)}} \tag{37}$$

Thus, in the αβz₁z₂ frame, the incoming-segment current linearly increases from zero to the target value $\boldsymbol{i}^{\mathrm{goal}}_{\alpha\beta\mathrm{z1z2(on)}}$.

IV. SEGMENT-SWITCHING STRATEGY

Based on the theoretical analysis in section III, this section first determines the two key current vectors, $\boldsymbol{i}_{\alpha\beta\mathrm{z1z2(off)}}(0)$ and $\boldsymbol{i}^{\mathrm{goal}}_{\alpha\beta\mathrm{z1z2(on)}}$, which critically govern the optimal switching time, the time-optimal voltage vector, and the corresponding current trajectory, according to the practical current control objectives. Following this, the conventional segmented-switching method is reviewed, and an improved segment-switching strategy based on time-optimal voltage feedforward is then proposed.

The vectors $\boldsymbol{i}_{\alpha\beta\mathrm{z1z2(off)}}(0)$ and $\boldsymbol{i}^{\mathrm{goal}}_{\alpha\beta\mathrm{z1z2(on)}}$ correspond to the thrust-related current reference values at the start and completion of the switching process, respectively. The αβ-subspace is associated with electromechanical energy conversion, where the α- and β-axis currents are typically regulated within the secondary-field-oriented control (SFOC) [25] framework via the Park transformation in the d-q synchronous rotating reference frame. Given the d- and q-axis current references i_{dref} and i_{qref}, the αβ-axis current references are determined by:

$$\begin{bmatrix} i_{\alpha\mathrm{ref}}\left(t\right) \\ i_{\beta\mathrm{ref}}\left(t\right) \end{bmatrix} = \begin{bmatrix} \cos\left(\theta\right) & -\sin\left(\theta\right) \\ \sin\left(\theta\right) & \cos\left(\theta\right) \end{bmatrix} \begin{bmatrix} i_{\mathrm{dref}} \\ i_{\mathrm{qref}} \end{bmatrix} \tag{38}$$

where θ is the angle between the secondary flux linkage vector and the α-axis. The z₁z₂-subspace is related to harmonic components, and its current references are set to zero:

$$i_{\mathrm{z1ref}}\left(t\right) = i_{\mathrm{z2ref}}\left(t\right) = 0 \tag{39}$$

For convenience, the switching start instant is defined as the time zero for the αβ-axis reference currents. Assuming the currents in all axes of the exiting segment accurately track their references before switching, the vector $\boldsymbol{i}_{\alpha\beta\mathrm{z1z2(off)}}(0)$ is:

$$\boldsymbol{i}_{\alpha\beta\mathrm{z1z2(off)}}\left(0\right) = \begin{bmatrix} i_{\alpha\mathrm{ref}}\left(0\right) & i_{\beta\mathrm{ref}}\left(0\right) & 0 & 0 \end{bmatrix}^{\mathrm{T}} \tag{40}$$

Substituting into (31) yields the minimum disconnection time:

$$t^*_{\mathrm{off}} = \sqrt{\left(L^2_{\alpha} + M^2_{\alpha\mathrm{z2}}\right) i^2_{\alpha\mathrm{ref}}\left(0\right) + L^2_{\beta} i^2_{\beta\mathrm{ref}}\left(0\right)} / U_{\mathrm{m}} \tag{41}$$

Under the condition of constant current magnitude, (42) holds:

$$i^2_{\alpha\mathrm{ref}}\left(t\right) + i^2_{\beta\mathrm{ref}}\left(t\right) = I^2_{\mathrm{mref}} \tag{42}$$

where I_{mref} is the reference current amplitude. Combining (42) with (41) gives:

$$t^*_{\mathrm{off}} = \frac{\sqrt{\left(L^2_{\alpha} + M^2_{\alpha\mathrm{z2}} - L^2_{\beta}\right) i^2_{\alpha\mathrm{ref}}\left(0\right) + L^2_{\beta} I^2_{\mathrm{mref}}}}{U_{\mathrm{m}}} \tag{43}$$

The vector $\boldsymbol{i}^{\mathrm{goal}}_{\alpha\beta\mathrm{z1z2(on)}}$ is the αβz₁z₂-axis reference current at time $t^*_{\mathrm{off}} + t^*_{\mathrm{on}}$, i.e.:

$$\boldsymbol{i}^{\mathrm{goal}}_{\alpha\beta\mathrm{z1z2(on)}} = \begin{bmatrix} i_{\alpha\mathrm{ref}}\left(t^*_{\mathrm{off}} + t^*_{\mathrm{on}}\right) & i_{\beta\mathrm{ref}}\left(t^*_{\mathrm{off}} + t^*_{\mathrm{on}}\right) & 0 & 0 \end{bmatrix}^{\mathrm{T}} \tag{44}$$

Substituting (44) into (35) and simplifying yields:

$$t^*_{\mathrm{on}} = \frac{\sqrt{\left(L^2_{\alpha} + M^2_{\alpha\mathrm{z2}} - L^2_{\beta}\right) i^2_{\alpha\mathrm{ref}}\left(t^*_{\mathrm{off}} + t^*_{\mathrm{on}}\right) + L^2_{\beta} I^2_{\mathrm{mref}}}}{U_{\mathrm{m}}} \tag{45}$$

Unlike t_{off}^*, which can be directly obtained from (41), (45) is a nonlinear equation in t_{on}^*. Numerical methods such as the Newton iteration can be employed for online real-time solution; the specific procedure is detailed in Appendix II.

Furthermore, based on (43) and (45), and considering that $i_{\alpha\text{ref}}(t)$ varies within the range [0, I_{mref}], the value ranges for t_{off}^* and t_{on}^* are obtained as:

$$L_\beta I_{\text{mref}}/U_{\text{m}} \le t_{\text{off}}^*, t_{\text{on}}^* \le L_\alpha I_{\text{mref}}/U_{\text{m}} \tag{46}$$

This provides a theoretical basis for estimating the segment-switching duration.

A. Conventional Segment-switching Strategy

The control block diagram of the conventional segment-switching strategy is shown in Fig. 4. In this strategy, both normal operation and the switching stage rely on SFOC for current regulation. Longitudinal static end-effect leads to six-phase current imbalance, inducing second-order harmonics in the d-q axis currents [26]. To suppress the resulting thrust pulsation, the system employs proportional-integral-resonant (PIR) controllers to track the d-q axis current references and attenuate this second harmonic component. Concurrently, the unbalanced six-phase currents introduce a fundamental frequency component in the z_1-z_2 subspace [27], which is suppressed using proportional-resonant (PR) controllers.

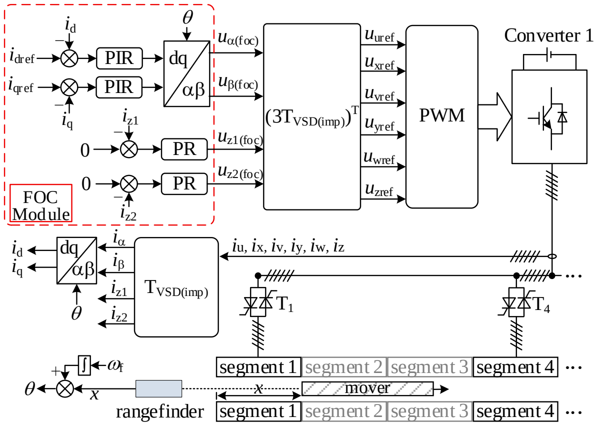

Fig. 4. Control block diagram of conventional segment-switching strategy.

In the conventional method, the triggering commands for the TRIACs are directly determined by the mover position x: upon detecting that the mover has just left a stator segment, the trigger signals for that segment's TRIACs are immediately removed, and the trigger commands for the incoming segment's TRIACs are simultaneously issued.

B. Proposed Segment-switching Strategy

The block diagram of the proposed segment-switching strategy is shown in Fig. 5. Compared to the conventional strategy, the proposed one introduces a "segment-switching module" in the reference voltage calculation. This module works in coordination with the original "field-oriented control (FOC) module" to achieve fast and smooth segment switching. The reference voltage is supplied by the "FOC module" during normal operation and by the "segment-switching module" during the switching process.

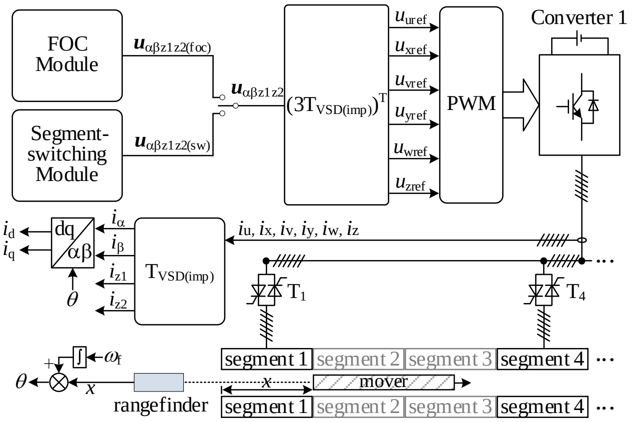

Fig. 5. Control block diagram of proposed segment-switching strategy.

The internal structure of the "segment-switching module" is shown in Fig. 6. Its output reference voltage $\boldsymbol{u}_{\alpha\beta z1z2(\text{sw})}$ is formed by a combination of the time-optimal feedforward voltage $\boldsymbol{u}_{\alpha\beta z1z2\text{fwd}}(t)$ and the outputs $\boldsymbol{u}_{\text{PI}}$ of the α- and β-axis current PI controllers, as shown in (47), to enhance system robustness:

$$\boldsymbol{u}_{\alpha\beta z1z2(\text{sw})}=\boldsymbol{u}_{\alpha\beta z1z2\text{fwd}}(t)+\boldsymbol{u}_{\text{PI}} \tag{47}$$

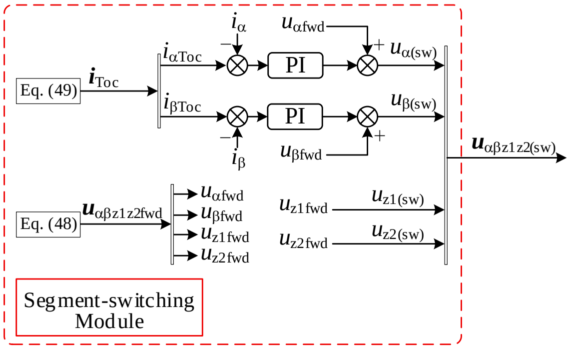

Fig. 6. The internal structure of the "segment-switching module" in the proposed segment-switching strategy.

where $\boldsymbol{u}_{\alpha\beta z1z2\text{fwd}}(t)$ is given by:

$$\boldsymbol{u}_{\alpha\beta z1z2\text{fwd}}(t)=\begin{cases}\boldsymbol{u}^*_{\alpha\beta z1z2(\text{off})}+R_s\boldsymbol{i}_{\alpha\beta z1z2}+\boldsymbol{u}_{\text{M}}, t\in\left[0,t^*_{\text{off}}\right)\\ \boldsymbol{u}^*_{\alpha\beta z1z2(\text{on})}+R_s\boldsymbol{i}_{\alpha\beta z1z2}+\boldsymbol{u}_{\text{M}}, t\in\left[t^*_{\text{off}}, t^*_{\text{off}}+t^*_{\text{on}}\right)\end{cases} \tag{48}$$

where $\boldsymbol{u}_{\text{M}}$ is the adjacent-segment mutual inductance voltage ((14)). The reference command for the α- and β-axis current proportional-integral (PI) controllers is the desired time-optimal current trajectory $\boldsymbol{i}_{\text{Toc}}(t)$, given by:

$$\boldsymbol{i}_{\text{Toc}}(t)=\begin{cases}\boldsymbol{i}_{\alpha\beta z1z2(\text{off})}(t), t\in\left[0,t^*_{\text{off}}\right)\\ \boldsymbol{i}_{\alpha\beta z1z2(\text{on})}(t), t\in\left[t^*_{\text{off}}, t^*_{\text{off}}+t^*_{\text{on}}\right)\end{cases} \tag{49}$$

The timing of the TRIACs trigger commands in the proposed strategy is also modified: When the mover leaves a segment, the trigger signals for that segment's TRIACs are removed immediately, but the trigger command for the incoming segment's TRIACs is issued after a delay equal to the optimal disconnection time t_{off}^*. The implementation flow of the proposed strategy (see flowchart in Fig. 7) is as follows:

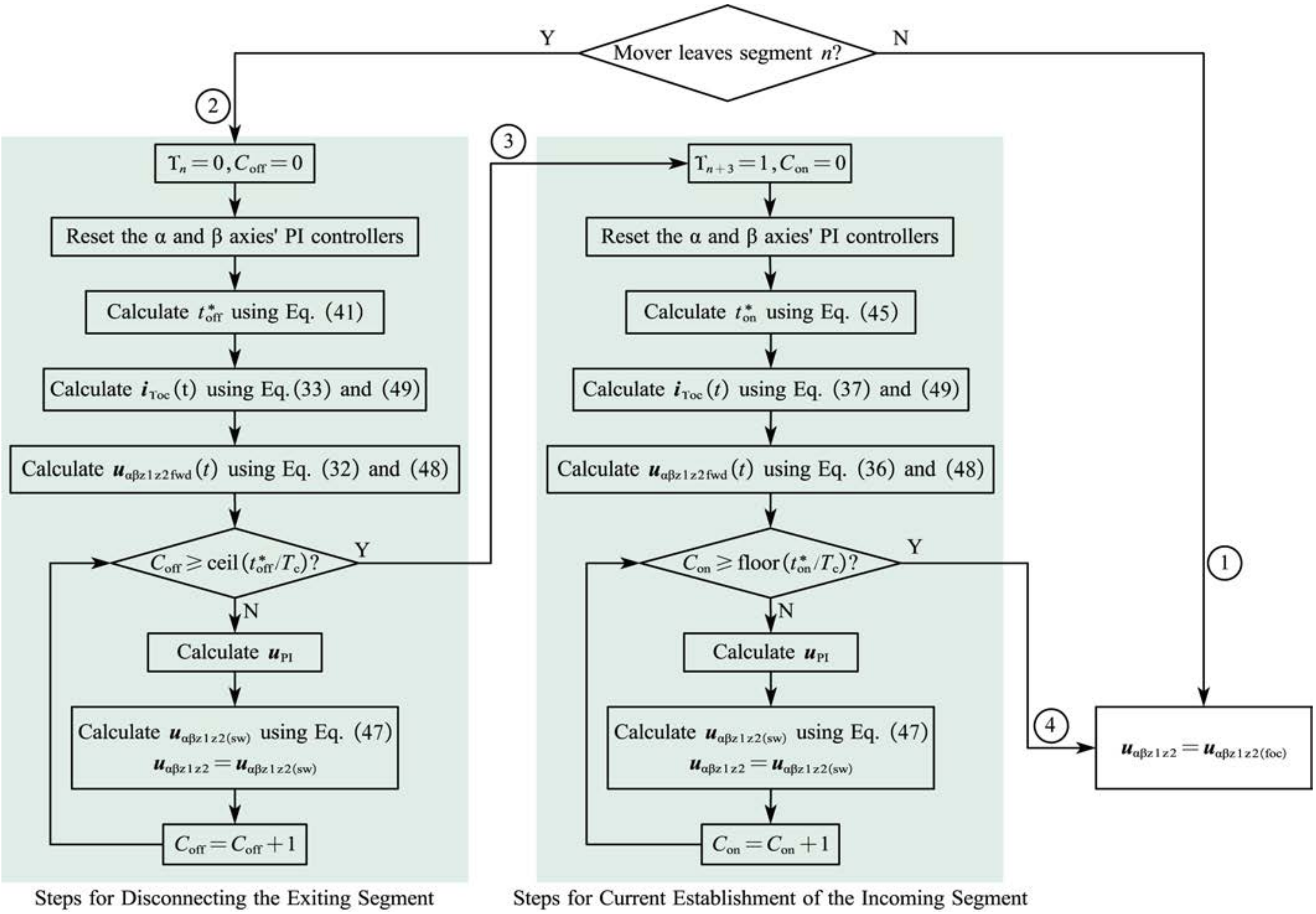

Fig. 7. Flowchart of the detailed implementation steps for proposed segment-switching method.

1) Normal feeding stage

During this stage, the mover has not yet left segment n, and the system operates identically to the conventional strategy. The $\alpha\beta z_1 z_2$-axis reference voltage $\boldsymbol{u}_{\alpha\beta z1z2}$ is directly taken from the output of the "FOC module", $\boldsymbol{u}_{\alpha\beta z1z2(\mathrm{foc})}$.

2) Exiting segment disconnection stage

This stage commences when the mover position signal indicates it has passed the boundary of segment n. The trigger signal to thyristor T_n is immediately removed. Simultaneously, the source of the $\alpha\beta z_1 z_2$-axis reference voltage is switched from the "FOC module" to the output of the "segment-switching module", thereby initiating the time-optimal current decay control for the exiting segment. The controller first initializes a counter (setting $C_{\mathrm{off}} = 0$) and resets the integrators of the α- and β-axis PI controllers. It then calculates the minimum disconnection time t_{off}^{*} using (41). Based on this result, the desired time-optimal current decay trajectory $\boldsymbol{i}_{\mathrm{Toc}}(t)$ for the α- and β-axes is generated according to (33) and (49), and the time-optimal feedforward voltage vector $\boldsymbol{u}_{\alpha\beta z1z2\mathrm{fwd}}(t)$ is derived from (32) and (48). Following these one-time setups, a closed-loop control cycle executes in every subsequent control period T_{c}: The PI controller outputs are calculated and fused with the feedforward voltage $\boldsymbol{u}_{\alpha\beta z1z2\mathrm{fwd}}(t)$ to form the final voltage command $\boldsymbol{u}_{\alpha\beta z1z2(\mathrm{sw})}$, and the counter C_{off} is incremented. This cycle repeats until C_{off} exceeds ceil(t_{off}^{*} $/T_{\mathrm{c}}$), indicating the exiting segment current has fully decayed to zero, where ceil(·) denotes the ceiling function that rounds a real number up to the nearest integer.

3) Incoming segment current establishment stage

This stage begins immediately upon confirmation that the exiting segment is fully disconnected. The trigger command is issued to thyristor T_{n+3}. A new counter is initialized (setting $C_{\mathrm{on}} = 0$), and the α- and β-axis PI controllers are reset. The minimum current establishment time t_{on}^{*} is then obtained by solving (45), typically using the Newton method. Employing this calculated t_{on}^{*}, the target current rise trajectory $\boldsymbol{i}_{\mathrm{Toc}}(t)$ is established via (37) and (49), and the corresponding time-optimal feedforward voltage $\boldsymbol{u}_{\alpha\beta z1z2\mathrm{fwd}}(t)$ is determined from (36) and (48). Subsequently, within each control period, a control loop analogous to the previous stage is performed: the PI controller outputs are calculated and combined with $\boldsymbol{u}_{\alpha\beta z1z2\mathrm{fwd}}(t)$ to generate the voltage command $\boldsymbol{u}_{\alpha\beta z1z2(\mathrm{sw})}$, while C_{on} is incremented. This process continues until C_{on} is greater than floor(t_{on}^{*} $/T_{\mathrm{c}}$), signifying that the incoming segment's current has risen sufficiently close to its target reference value under the SFOC framework, where floor(·) denotes the floor function that rounds a real number down to the nearest integer.

4) Return to normal feeding stage

Once the incoming segment's currents are established, the system transitions back to standard FOC-based operation. The feedback signals for all controllers within the “FOC module” (namely, the d-q axis PIR and z_1z_2 axis PR controllers) are restored to their actual sampled values. Concurrently, the source for the $\alpha\beta z_1z_2$-axis reference voltage is switched back to the output of the “FOC module”. This completes the entire fast and smooth segment-switching process between Segment *n* and Segment (*n*+3).

It is important to note that a special treatment is applied to the “FOC module” during switching stages ② and ③: The feedback values for the d-q axis PIR controllers and the z_1z_2 axis PR controllers are forcibly set to their respective reference values (Fig. 8). This zeroes the controller inputs, effectively locking their outputs at the steady-state values from the start of the switching process. Actual feedback is restored at the end of the switching process (stage ④). The rationale is that the system operates under the same no-load condition (uncoupled from the mover) at both the start and end of the switching process. Furthermore, because of the extremely short switching duration, the synchronous angular frequency and load-impedance characteristics can be considered constant. Consequently, the steady-state voltage demand is identical at both instants. This method avoids the re-integration settling process of the controllers when switching back from the “segment-switching module” to the “FOC module”, thereby improving the system’s dynamic performance.

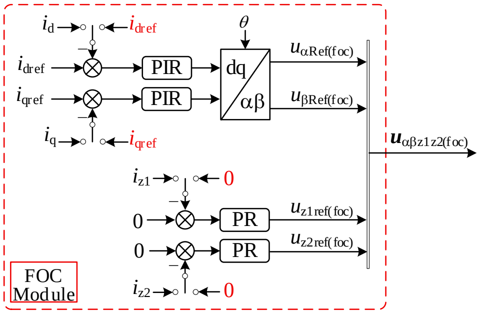

Fig. 8. The internal structure of the “FOC module” in the proposed segment-switching strategy.

V. EXPERIMENT AND SIMULATION VERIFICATION

Section V aims to validate the effectiveness of the proposed segment-switching strategy. Due to experimental constraints, the maximum design speed of the mover in the prototype is 6 m/s. Therefore, the experimental study focuses on evaluating the control performance of the segment-switching transient current during the acceleration of the mover from standstill to 6 m/s. For higher speed conditions (i.e., accelerating the mover from standstill to 420 m/s), the effectiveness of the proposed segment-switching strategy is verified through simulations.

A. *Experimental Setup*

A prototype of a segmented long-stator linear induction motor drive system was developed in the laboratory. Fig. 9(a) shows a photograph of the long-stator linear motor. Its stator is assembled from 16 equally long stator segments aligned along the direction of motion. Each stator segment employs dual-Y shift 30° windings, and its six-phase supply lines are connected to the power source via TRIACs. A laser distance sensor is mounted at the leading end of the stator to detect the mover position in real time. The mover, made of an aluminum plate, has a length approximately 1.5 times that of a single stator segment.

The power supply and control system are shown in Fig. 9(b), which mainly consists of a direct current (DC) voltage source, three converters, three current-sensing boards, a host PC, and a communication and control unit. The DC voltage source provides the common DC-link voltage for the converters. Each converter has six legs to supply a six-phase AC voltage to the stator segments. The currents of the three converters are measured by independent current-sensing boards. The host PC is used to send start/stop and reset commands to the controller, while the communication and control unit is responsible for collecting and transmitting the sampled signals and for the real-time execution of the control algorithm.

The six-phase inductance matrix of the stator segment under no-load conditions is listed in Table I. By applying the improved VSD transformation to this matrix, the inductance values in the $\alpha\beta z_1z_2$ subspace are obtained and presented in Table II. And the other specific parameters of the experimental platform and the controller design are also listed in Table II. The maximum control voltage U_m is set to 0.8 U_{limit}, which reserves a portion of the voltage margin to compensate for the resistance voltage drop, the mutual

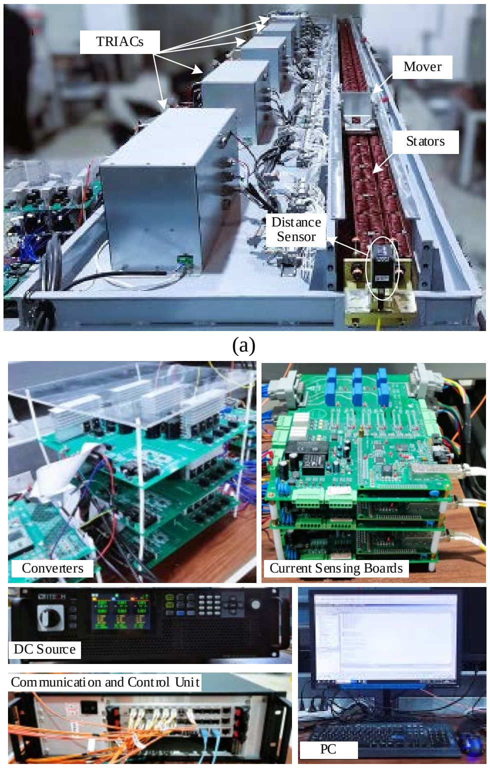

(a)

(b)

Fig. 9. Photograph of the experimental setup. (a) Prototype of the segmented long-stator linear induction motor. (b) The power supply and control system.

inductance voltage from adjacent segments, and the potential compensation output of the PI controller. In addition, it is important to note that the same PIR (d-q axes) and PI (z_1z_2 axes) controller parameters (listed in Table II) were used for both the conventional and proposed switching methods to guarantee a fair comparison.

TABLE I
INDUCTANCE MATRIX ELEMENTS OF THE SIX-PHASE STATOR SEGMENT

Phase	U	X	W	Z	V	Y
U/mH	4.147	2.199	−1.539	−0.923	0.280	−0.360
X/mH	2.199	4.174	−2.218	−1.567	0.959	0.323
W/mH	−1.539	−2.218	4.156	2.212	−1.536	−0.880
Z/mH	−0.923	−1.567	2.212	4.119	−2.196	−1.522
V/mH	0.280	0.959	−1.536	−2.196	4.205	2.264
Y/mH	−0.360	0.323	−0.880	−1.522	2.264	4.190

TABLE II
PARAMETERS OF THE EXPERIMENTAL PROTOTYPE

Parameter	Value
Pole pitch/mm	60
Stator segment length, l_s/mm	240
Mover length/mm	360
The max velocity/(m·s^{-1})	6
Max phase voltage of converter, U_{limit}/V	67.5
Rated and reference current amplitude, I_{mref}/A	10
Phase resistance of stator segment/Ω	1.71
L_α/mH	9.826
L_β/mH	5.396
L_{z1}/mH	0.968
L_{z2}/mH	1.280
$M_{\alpha z2}$/mH	1.168
L_{dc}/mH	0.876
Control period/μs	100
Parameters of the d-q axes current PIR controllers, k_p, k_i, k_r	6480, 100
Parameters of the z_1z_2 axes current PR controllers, k_p, k_r	0.5, 100
Parameters of the αβ axes current PI controllers, k_p, k_i	2240
The maximum control voltage, U_m	$0.8U_{\text{limit}}$

B. *Experimental Results*

Take Converter 1 among the three converters as an example to compare and analyze the two segment-switching strategies. Fig. 10(a) shows the current waveform of Converter 1 under the conventional switching method, which involves four segment-switching transients. The corresponding current overshoots during these transients are 11.69%, 26.10%, 30.40%, and 32.70%, respectively. Fig. 10(b) presents the current waveform of Converter 1 when the proposed switching strategy is applied. It can be observed that, with the proposed strategy, the current overshoots during the first and third segment-switching transients are 4.50% and 5.50%, respectively, while those during the second and fourth transients are negligible.

Take the current during the third segment-switching transient as an example to further illustrate the specific transient characteristics of the two segment-switching strategies. Fig. 11(a) shows, from top to bottom, the exiting segment current, the incoming segment current, and the converter current (i.e., the sum of the exiting and incoming segment currents) during the third switching transient in Fig. 10 under the conventional segment-switching method. Fig. 11(b) presents the corresponding currents under the proposed segment-switching strategy.

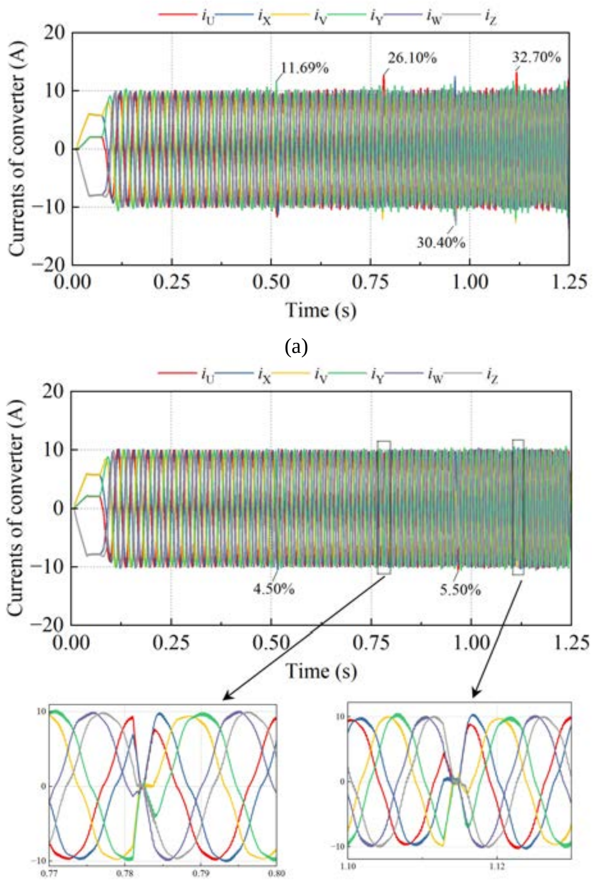

(a)

(b)

Fig. 10. The current waveform of Converter 1 during the acceleration of the mover from standstill to 6 m/s. (a) With the conventional segment-switching method. (b) With the proposed segment-switching method.

As shown in Fig. 11(a), under the conventional segment-switching method, the incoming segment is engaged immediately at the start of the switching transient. However, due to the natural zero-current turn-off characteristic of thyristors, the exiting segment cannot be disconnected from Converter 1 instantaneously, resulting in a parallel connection of the two segments. This parallel state causes a sudden change in the equivalent load impedance, which in turn induces a noticeable current overshoot in the converter, reaching 30.40% as indicated in Fig. 11(a). The six-phase current of the exiting segment takes about 6.2 ms to decay to zero, during which the parallel connection persists. Consequently, the incoming segment current, being disturbed by the exiting segment current, cannot be accurately regulated to its target value within 6.2 ms.

In contrast, as shown in Fig. 11(b), under the proposed segment-switching method, the incoming segment is only engaged after the exiting segment has been disconnected from Converter 1, thereby avoiding any parallel connection. The regulation of the incoming segment current is therefore free from interference by the current of the other segment. It can be observed that the proposed segment-switching strategy reduces the exiting segment current to zero within approximately 1.8 ms, which is much shorter than the 6.2 ms required by the conventional segment-switching method, thus reserving relatively ample time for the subsequent regulation of the incoming segment current. Furthermore, substituting the experimental parameters into (46) yields the following theoretical prediction range for the turn-off time: $5.396\times10/(67.5\times0.8)\ \text{s} < t_{\text{off}}^{*} < 9.826\times10/(67.5\times0.8)\ \text{s}$, and the experimentally measured value of about 1.8 ms falls within this range, agreeing well with the theoretical result.

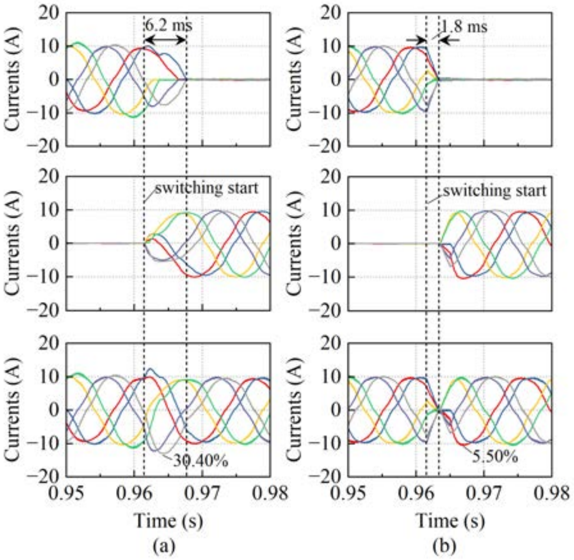

Fig. 11. The current waveforms of the exiting segment, the incoming segment, and the converter during the third segment-switching transient. (a) With the conventional segment-switching method. (b) With the proposed segment-switching method.

To intuitively compare the settling time of the two segment-switching methods, Fig. 12 shows the waveforms of i_α, i_β, i_{z1}, and i_{z2} (i.e., the α-, β-, z_1-, and z_2-axis currents of Converter 1) along with their references during the third segment-switching transient. The αβ-axis reference currents $i_{\alpha\text{ref}}$ and $i_{\beta\text{ref}}$ are obtained by Park transformation from the dq-axis reference currents, whereas the references for the z_1-z_2 axis currents are zero and are therefore not plotted in the figure. As can be seen, before the start of the segment switching, i_α and i_β accurately track their references, while i_{z1} and i_{z2} remain close to zero. During the switching transient, the conventional switching strategy requires about 7.2 ms for i_α, i_β, i_{z1}, and i_{z2} to regain reference tracking, whereas the proposed strategy needs about 4.4 ms (the fundamental period of the current is approximately 16.2 ms, as shown in Fig. 12; therefore, the time from the start of switching to reaching the target current is about 27.16% of the fundamental period), thereby reducing the settling time by 38.89%.

Fig. 13 shows the distance and velocity curves of the mover during operation under the two segment-switching strategies. The velocity curves are obtained by differentiating the displacement curves with respect to time, and therefore exhibit considerable fluctuations. Nevertheless, it can be observed that the distance and velocity curves under the two segment-switching strategies almost completely coincide. This indicates that the proposed segment-switching strategy does not adversely affect the acceleration performance of the mover while mitigating the current overshoot issue of the conventional method.

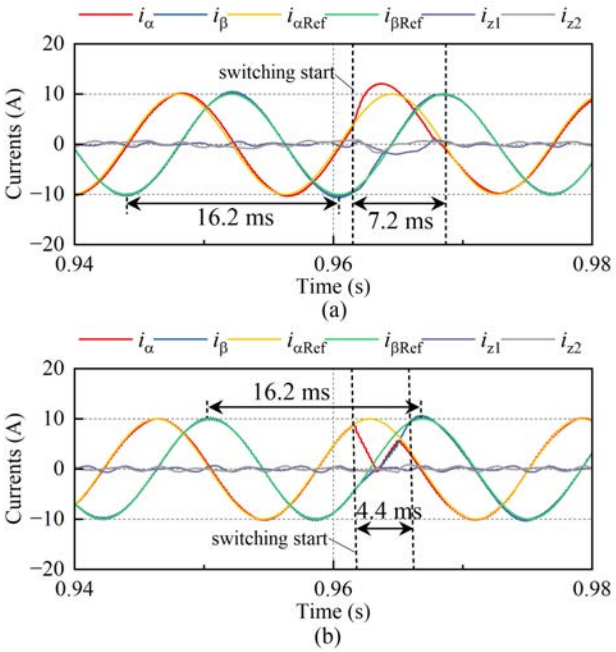

Fig. 12. The waveforms the α-, β-, z_1-, and z_2-axis currents of Converter 1 along with their references during the third segment-switching transient. (a) With the conventional segment-switching method. (b) With the proposed segment-switching method.

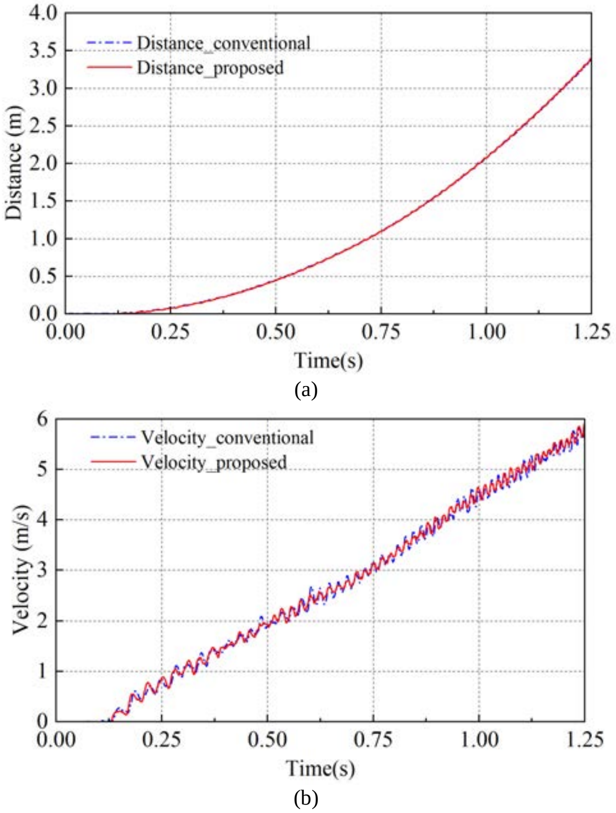

Fig. 13. The experimentally obtained distance and velocity curves under the two segment-switching strategies. (a) Distance curves. (b) Velocity curves.

C. Simulation Results

The simulation model still adopts three converters for a segmented power supply to the linear motor, and the specific parameters of the simulation model are listed in Table III.

TABLE III
PARAMETERS OF THE SIMULATION

Parameter	Value
Pole pitch/m	0.40
Stator segment length, l_s/m	3.20
Mover length/m	4.80
Phase resistance of stator segment/Ω	0.1
L_α/mH	0.799
L_β (mH)	0.600
L_{z1} (mH)	0.150
L_{z2} (mH)	0.164
$M_{\alpha z2}$ (mH)	0.053
L_{dc} (mH)	0.040
Max phase voltage of converter, U_{limit} (kV)	13
The maximum control voltage, U_m	$0.8U_{imit}$
Reference current amplitude, I_{mref} (kA)	5
Control period (μs)	100
Parameters of the d-q axes current PIR controllers, k_p, k_i, k_r	1.88, 314, and 80
Parameters of the z_1z_2 axes current PR controllers, k_p, k_r	1.5, 80
Parameters of the αβ axes current PI controllers, k_p, k_i	2, 300

Fig. 14(a) shows the current waveform of Converter 1 under the conventional switching method during the acceleration of the mover from standstill to 420 m/s, which involves several segment-switching transients. The maximum current overshoot during these transients reaches 37.06%. Fig. 14(b) presents the current waveform of Converter 1 when the proposed switching strategy is applied. It can be observed that, with the proposed strategy, the maximum current overshoot is only 5.44%.

Take a segment-switching transient that occurs between 2.003 and 2.009 s (when the mover speed is approximately 320 m/s) as an example to illustrate the specific transient characteristics of the two segment-switching strategies. Fig. 15(a) shows, from top to bottom, the exiting segment current, the incoming segment current, and the converter current during this switching transient under the conventional segment-switching method. Fig. 15(b) presents the corresponding currents under the proposed segment-switching strategy. As shown in Fig. 15(a), under the conventional segment-switching method, the six-phase current of the exiting segment takes about 0.95 ms to decay to zero, and the current overshoot of the converter reaches 30.40%. In contrast, as shown in Fig. 15(b), the proposed segment-switching strategy reduces the exiting segment current to zero within approximately 0.38 ms, which is 40% of the time required by the conventional method. Furthermore, substituting the simulation parameters into (46) yields the following theoretical prediction range for the turn-off time: $0.799\times10^{-3}\times5000/(13000\times0.8)$ s < t^*_{off} < $0.600\times10^{-3}\times5000/(13000\times0.8)$ s, and the simulation result of about 0.38 ms falls within this range, agreeing well with the theoretical result.

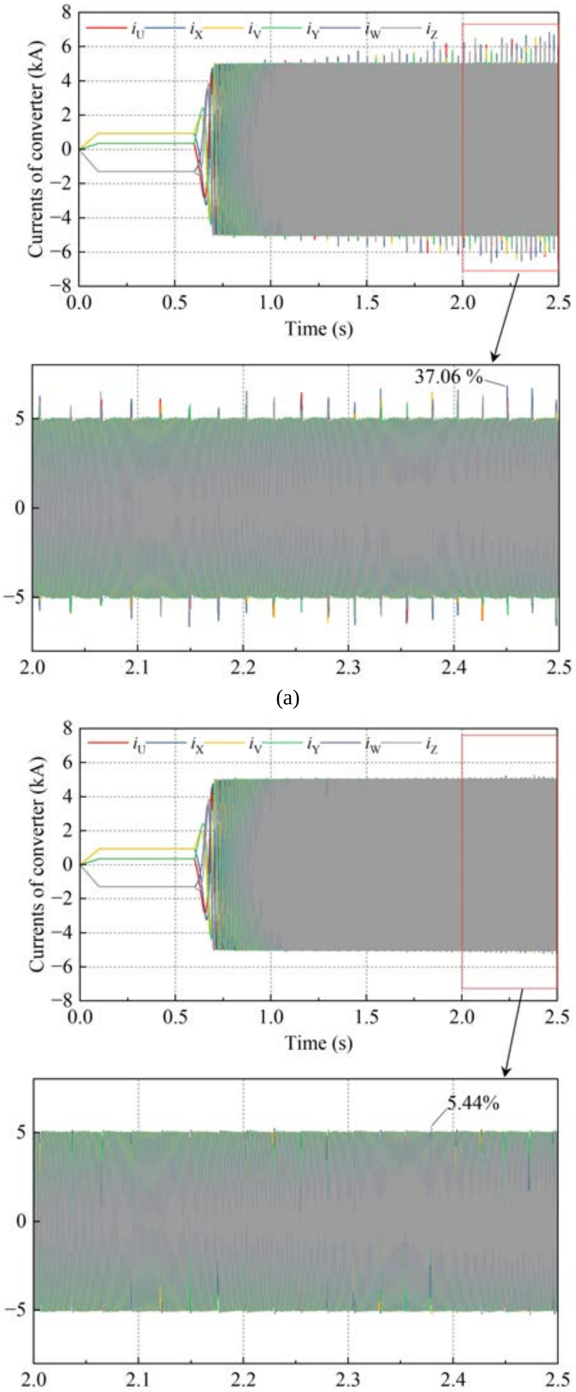

(a)

(b)

Fig. 14. The current waveform of Converter 1 during the acceleration of the mover from standstill to 420 m/s. (a) Under the conventional switching method. (b) Under the proposed switching method.

To compare the settling time of the two segment-switching methods, Fig. 16 shows the waveforms of the α-, β-, z_1-, and z_2-axis currents of Converter 1 from 2.003 to 2.009 s. As can be seen, after the switching starts, the conventional switching strategy requires about 2.5 ms for i_α, i_β, i_{z1}, and i_{z2} to regain reference tracking, whereas the proposed strategy takes only about 1.5 ms (the fundamental period of the current is approximately 2.5 ms, as shown in Fig. 16), thereby reducing the settling time by 40%.

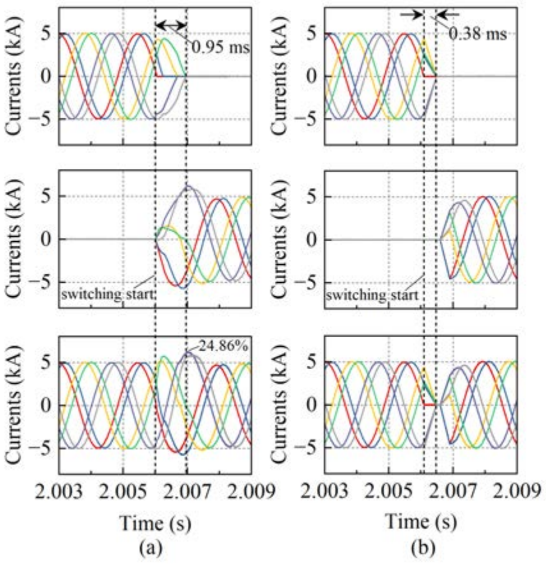

(a) (b)

Fig. 15. The current waveforms of the exiting segment, the incoming segment, and the converter from 2.003 to 2.009 s. (a) With the conventional segment-switching method. (b) With the proposed segment-switching method.

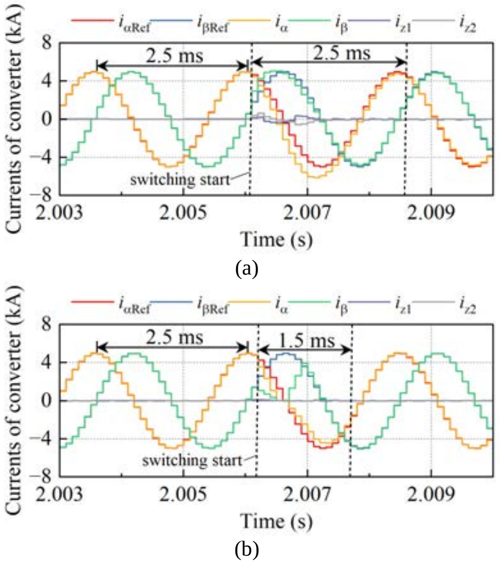

(a)

(b)

Fig. 16. The waveforms of the $\alpha\beta z_1 z_2$ currents of Converter 1 from 2.003 to 2.009 s. (a) Under the conventional switching method. (b) Under the proposed switching method.

Fig. 17 shows the simulated distance and velocity curves under the two segment-switching strategies. It can be observed that the two distance curves, as well as the two velocity curves, almost completely coincide. As shown in Fig. 17, when the later stage of the operation is examined with a magnified view, both the velocity and distance under the proposed segment-switching strategy are slightly larger than those under the conventional method, which is attributed to the shorter time required by the proposed strategy to regain reference current tracking. This indicates that, even under high-speed conditions, the proposed segment-switching strategy still does not adversely affect the acceleration performance of the mover while mitigating the current overshoot issue of the conventional method.

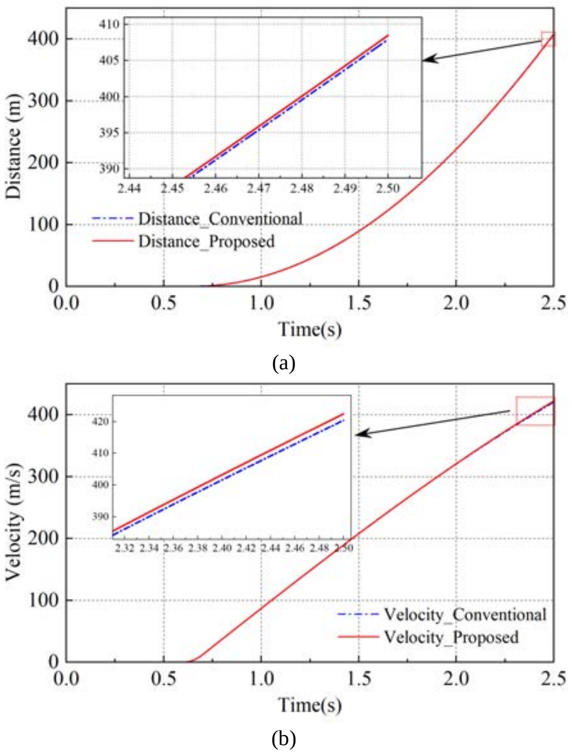

(a)

(b)

Fig. 17. The simulated distance and velocity curves under the two segment-switching strategies. (a) Distance curves. (b) Velocity curves.

VI. CONCLUSION

This paper establishes a mathematical model of a segmented long-stator linear motor that accounts for static longitudinal end-effect for segment switching. Based on time-optimal control theory, the minimum time required for disconnecting the exiting segment and for establishing the current in the incoming segment, as well as the corresponding time-optimal voltage and current trajectories, are derived analytically. A novel segment switching strategy with the current transient overshoot suppression based on time-optimal control theory is proposed. Experimental and simulation results collectively validate the effectiveness of the proposed segment-switching strategy. Under the experimental condition where the mover accelerates from standstill to 6 m/s, the maximum transient current overshoot of the conventional strategy is approximately 32.70%, whereas that of the proposed strategy is only 5.50%. Under the simulation condition of acceleration to 420 m/s, the maximum overshoot of the conventional strategy is 37.06%, compared to 5.44% for the proposed strategy. Moreover, the displacement and velocity curves under the two strategies almost completely coincide. These results indicate that the proposed strategy mitigates the current overshoot issue of the conventional method without adversely affecting the acceleration performance of the mover.

APPENDIX I

The conventional VSD transformation (excluding the $0_1 0_2$ axes) is:

$$\boldsymbol{T}_{\mathrm{VSD}}=\frac{1}{3}\begin{bmatrix} 1 & \frac{\sqrt{3}}{2} & -\frac{1}{2} & -\frac{\sqrt{3}}{2} & -\frac{1}{2} & 0 \\ 0 & \frac{1}{2} & \frac{\sqrt{3}}{2} & \frac{1}{2} & -\frac{\sqrt{3}}{2} & -1 \\ 1 & -\frac{\sqrt{3}}{2} & -\frac{1}{2} & \frac{\sqrt{3}}{2} & -\frac{1}{2} & 0 \\ 0 & \frac{1}{2} & -\frac{\sqrt{3}}{2} & \frac{1}{2} & \frac{\sqrt{3}}{2} & -1 \end{bmatrix}=\begin{bmatrix} \boldsymbol{v}_1 \\ \boldsymbol{v}_2 \\ \boldsymbol{v}_3 \\ \boldsymbol{v}_4 \end{bmatrix} \tag{A1}$$

After conventional VSD transformation, $\boldsymbol{L}_{\mathrm{s(sy)}}$ can be diagonalized as:

$$\begin{aligned}&\boldsymbol{T}_{\mathrm{VSD}}\boldsymbol{L}_{\mathrm{s(sy)}}\left(3\boldsymbol{T}_{\mathrm{VSD}}\right)^{\mathrm{T}}= \\ &\mathrm{diag}\left(L_{\mathrm{s\alpha\beta(sy)}},L_{\mathrm{s\alpha\beta(sy)}},L_{\mathrm{sz(sy)}},L_{\mathrm{sz(sy)}}\right)\end{aligned} \tag{A2}$$

where:

$$\begin{cases} L_{\mathrm{s\alpha\beta(sy)}}=L_0-M_{120}+\sqrt{3}/2\left(M_{30}-M_{150}\right) \\ L_{\mathrm{sz(sy)}}=L_0-M_{120}+\sqrt{3}/2\left(M_{150}-M_{30}\right) \end{cases} \tag{A3}$$

Given the special form of $\boldsymbol{L}_{\mathrm{s(asy)}}$ as shown in (3), before performing the conventional VSD transformation on $\boldsymbol{L}_{\mathrm{s(asy)}}$, express it in the following form:

$$\boldsymbol{L}_{\mathrm{s(asy)}}=L_{\mathrm{dc}}\boldsymbol{u}\boldsymbol{u}^{\mathrm{T}} \tag{A4}$$

where:

$$\boldsymbol{u}=\begin{bmatrix} 1 & 1 & 1 & 1 & -1 & -1 \end{bmatrix}^{\mathrm{T}} \tag{A5}$$

Then, after conventional VSD transformation, $\boldsymbol{L}_{\mathrm{s(asy)}}$ can be expressed as:

$$\begin{aligned}&\boldsymbol{T}_{\mathrm{VSD}}\boldsymbol{L}_{\mathrm{s(asy)}}\left(3\boldsymbol{T}_{\mathrm{VSD}}\right)^{\mathrm{T}}=\boldsymbol{T}_{\mathrm{VSD}}\left(L_{\mathrm{dc}}\boldsymbol{u}\boldsymbol{u}^{\mathrm{T}}\right)\left(3\boldsymbol{T}_{\mathrm{VSD}}\right)^{\mathrm{T}} \\ &=3L_{\mathrm{dc}}\boldsymbol{T}_{\mathrm{VSD}}\boldsymbol{u}\left(\boldsymbol{T}_{\mathrm{VSD}}\boldsymbol{u}\right)^{\mathrm{T}}=3L_{\mathrm{dc}}\boldsymbol{b}\boldsymbol{b}^{\mathrm{T}}\end{aligned} \tag{A6}$$

where:

$$\boldsymbol{b}=\boldsymbol{T}_{\mathrm{VSD}}\boldsymbol{u}=\begin{bmatrix} \boldsymbol{v}_1 \\ \boldsymbol{v}_2 \\ \boldsymbol{v}_3 \\ \boldsymbol{v}_4 \end{bmatrix}\boldsymbol{u}=\begin{bmatrix} b_1 \\ b_2 \\ b_3 \\ b_4 \end{bmatrix}=\begin{bmatrix} \frac{\sqrt{6}+\sqrt{2}}{3}\cos\left(\frac{5\pi}{12}\right) \\ \frac{\sqrt{6}+\sqrt{2}}{3}\sin\left(\frac{5\pi}{12}\right) \\ \frac{\sqrt{6}-\sqrt{2}}{3}\cos\left(\frac{\pi}{12}\right) \\ \frac{\sqrt{6}-\sqrt{2}}{3}\sin\left(\frac{\pi}{12}\right) \end{bmatrix} \tag{A7}$$

From (A6), it follows that if $\boldsymbol{b}$ contains as many zero entries as possible, then after transformation, $\boldsymbol{L}_{\mathrm{s(asy)}}$ will be simplified to the greatest extent (i.e., containing as many zero entries as possible). Note that $\boldsymbol{v}_1$ and $\boldsymbol{v}_2$ correspond to the same eigenvalue $L_{\mathrm{s\alpha\beta(sy)}}$, $\boldsymbol{v}_3$ and $\boldsymbol{v}_4$ correspond to the same eigenvalue $L_{\mathrm{sz\alpha\beta(sy)}}$. Therefore, if two different linear combinations of $\boldsymbol{v}_1$ and $\boldsymbol{v}_2$, together with two different linear combinations of $\boldsymbol{v}_3$ and $\boldsymbol{v}_4$ are chosen as the new eigenvectors of $\boldsymbol{L}_{\mathrm{s(sy)}}$ to form an improved transformation matrix $\boldsymbol{T}_{\mathrm{VSD(imp)}}$, then the transformed result of $\boldsymbol{L}_{\mathrm{s(sy)}}$ remains unchanged (still a diagonal matrix). However, this provides a possibility for simplifying $\boldsymbol{L}_{\mathrm{s(asy)}}$. As shown in the following equation, a single rotation applied to $[b_1,\ b_2]^{\mathrm{T}}$ suffices to introduce a zero entry.

$$\begin{bmatrix} \cos\left(\frac{5\pi}{12}\right) & \sin\left(\frac{5\pi}{12}\right) \\ -\sin\left(\frac{5\pi}{12}\right) & \cos\left(\frac{5\pi}{12}\right) \end{bmatrix}\begin{bmatrix} b_1 \\ b_2 \end{bmatrix}=\frac{1}{3}\begin{bmatrix} \sqrt{6}+\sqrt{2} \\ 0 \end{bmatrix} \tag{A8}$$

Substituting $[b_1,\ b_2]^{\mathrm{T}}=[\boldsymbol{v}_1,\ \boldsymbol{v}_2]^{\mathrm{T}}\boldsymbol{u}$ into the above equation, then:

$$\begin{bmatrix} \cos\left(\frac{5\pi}{12}\right) & \sin\left(\frac{5\pi}{12}\right) \\ -\sin\left(\frac{5\pi}{12}\right) & \cos\left(\frac{5\pi}{12}\right) \end{bmatrix}\begin{bmatrix} \boldsymbol{v}_1 \\ \boldsymbol{v}_2 \end{bmatrix}\boldsymbol{u}=\frac{1}{3}\begin{bmatrix} \sqrt{6}+\sqrt{2} \\ 0 \end{bmatrix} \tag{A9}$$

Thus, the new eigenvectors $\boldsymbol{v}_1'$ and $\boldsymbol{v}_2'$ are given by:

$$\begin{bmatrix} \boldsymbol{v}_1' \\ \boldsymbol{v}_2' \end{bmatrix}=\begin{bmatrix} \cos\left(\frac{5\pi}{12}\right) & \sin\left(\frac{5\pi}{12}\right) \\ -\sin\left(\frac{5\pi}{12}\right) & \cos\left(\frac{5\pi}{12}\right) \end{bmatrix}\begin{bmatrix} \boldsymbol{v}_1 \\ \boldsymbol{v}_2 \end{bmatrix} \tag{A10}$$

Similarly, by applying the rotation transformation shown in the following equation to $[b_3,\ b_4]^{\mathrm{T}}$, a zero entry can be introduced.

$$\begin{bmatrix} \cos\left(-\frac{5\pi}{12}\right) & \sin\left(-\frac{5\pi}{12}\right) \\ -\sin\left(-\frac{5\pi}{12}\right) & \cos-\left(\frac{5\pi}{12}\right) \end{bmatrix}\begin{bmatrix} b_3 \\ b_4 \end{bmatrix}=\frac{1}{3}\begin{bmatrix} 0 \\ \sqrt{6}-\sqrt{2} \end{bmatrix} \tag{A11}$$

Thus, the new eigenvectors $\boldsymbol{v}_3'$ and $\boldsymbol{v}_4'$ are given by:

$$\begin{bmatrix} \boldsymbol{v}_3' \\ \boldsymbol{v}_4' \end{bmatrix}=\begin{bmatrix} \cos\left(-\frac{5\pi}{12}\right) & \sin\left(-\frac{5\pi}{12}\right) \\ -\sin\left(-\frac{5\pi}{12}\right) & \cos-\left(\frac{5\pi}{12}\right) \end{bmatrix}\begin{bmatrix} \boldsymbol{v}_3 \\ \boldsymbol{v}_4 \end{bmatrix} \tag{A12}$$

The improved VSD transformation matrix $\boldsymbol{T}_{\mathrm{VSD(imp)}}$ can be obtained as:

$$\boldsymbol{T}_{\mathrm{VSD(imp)}}=\begin{bmatrix} \cos\left(\frac{5\pi}{12}\right) & \sin\left(\frac{5\pi}{12}\right) & 0 & 0 \\ -\sin\left(\frac{5\pi}{12}\right) & \cos\left(\frac{5\pi}{12}\right) & 0 & 0 \\ 0 & 0 & \cos\left(-\frac{5\pi}{12}\right) & \sin\left(-\frac{5\pi}{12}\right) \\ 0 & 0 & -\sin\left(-\frac{5\pi}{12}\right) & \cos\left(-\frac{5\pi}{12}\right) \end{bmatrix}\boldsymbol{T}_{\mathrm{VSD}} \tag{A13}$$

APPENDIX II

Numerical solution of a real-time online numerical solution procedure for t_{on}^{*} using Newton’s iteration method:

Considering the extremely short duration of the segment-switching process, the change in the stator current angular frequency ω_{e} during this period can reasonably be ignored. Multiplying both sides of (45) by ω_{e} yields:

$$\begin{aligned}\theta_{\mathrm{on}}&=\omega_{\mathrm{e}}t_{\mathrm{on}}^{*} \\ &=\frac{\omega_{\mathrm{e}}\sqrt{\left(L_{\alpha}^{2}+M_{\alpha z2}^{2}-L_{\beta}^{2}\right)i_{\alpha\mathrm{ref}}^{2}\left(t_{\mathrm{off}}^{*}+t_{\mathrm{on}}^{*}\right)+L_{\beta}^{2}I_{\mathrm{mref}}^{2}}}{U_{\mathrm{m}}}\end{aligned} \tag{B1}$$

where $i_{\alpha\mathrm{ref}}(t_{\mathrm{off}}^{*}+t_{\mathrm{on}}^{*})$ can be expressed as:

$$i_{\alpha\mathrm{ref}}\left(t_{\mathrm{off}}^{*}+t_{\mathrm{on}}^{*}\right)=I_{\mathrm{mref}}\cos\left(\varphi+\theta_{\mathrm{on}}\right) \tag{B2}$$

Here, φ is the phase of $i_{\alpha\mathrm{ref}}$ at time t_{off}^{*}, specifically:

$$\varphi=\arctan\left(i_{\mathrm{qref}}/i_{\mathrm{dref}}\right)+\theta_{\mathrm{d}}\left(t_{\mathrm{off}}^{*}\right) \tag{B3}$$

where $\theta_{\mathrm{d}}(t_{\mathrm{off}}^{*})$ is the spatial phase angle of the d-axis of the synchronous rotating frame at time t_{off}^{*}. Substituting (B2) into (B1) and rearranging yields a nonlinear equation for θ_{on}:

$$\begin{aligned}f\left(\theta_{\mathrm{on}}\right)=&\left(\frac{U_{\mathrm{m}}}{\omega_{\mathrm{e}}I_{\mathrm{mref}}}\right)^{2}\theta_{\mathrm{on}}^{2}-\\&\left(L_{\alpha}^{2}+M_{\alpha z2}^{2}-L_{\beta}^{2}\right)\cos^{2}\left(\varphi+\theta_{\mathrm{on}}\right)+L_{\beta}^{2}=0\end{aligned} \tag{B4}$$

Newton's iteration method is employed to numerically solve (B4), with the iteration equation given by:

$$\theta_{\mathrm{on}}^{(k+1)}=\theta_{\mathrm{on}}^{(k)}-f\left(\theta_{\mathrm{on}}^{(k)}\right)/f'\left(\theta_{\mathrm{on}}^{(k)}\right) \tag{B5}$$

where:

$$\begin{aligned}&f'\left(\theta_{\mathrm{on}}^{(k)}\right)=\\&2\left(\frac{U_{\mathrm{m}}}{\omega_{\mathrm{e}}I_{\mathrm{mref}}}\right)^{2}\theta_{\mathrm{on}}^{(k)}+\left(L_{\alpha}^{2}+M_{\alpha z2}^{2}-L_{\beta}^{2}\right)\sin\left(2\theta_{\mathrm{on}}^{(k)}+2\varphi\right)\end{aligned} \tag{B6}$$

The iteration continues until the convergence criterion is satisfied:

$$\left|\theta_{\mathrm{on}}^{(k+1)}-\theta_{\mathrm{on}}^{(k)}\right|<0.0001 \tag{B7}$$

Once the numerical solution is obtained, t_{on}^{*} is given by:

$$t_{\mathrm{on}}^{*}=\theta_{\mathrm{on}}^{*}/\omega_{\mathrm{e}} \tag{B8}$$

REFERENCES

[1] R. W. Cao, Y. Jin, and M. H. Lu *et al*., "Quantitative Comparison of Linear Flux-switching Permanent Magnet Motor with Linear Induction Motor for Electromagnetic Launch System," *IEEE Transactions on Industrial Electronics*, vol. 65, no. 9, pp. 7569–7578, Sept. 2018.

[2] J. Y. Lu, and W. M. Ma, "Research on End Effect of Linear Induction Machine for High-speed Industrial Transportation," *IEEE Transactions on Plasma Science*, vol. 39, no. 1, pp. 116–120, Jan. 2011.

[3] J. Q. Zhu, X. Q. Cao, and Q. X. Ge *et al*., "Adaptive-SMO-Based Traction Force Fluctuation Suppression Strategy Considering Suspension System for High-speed Maglev Train," *IEEE Transactions on Industrial Electronics*, vol. 71, no. 3, pp. 2289–2299, Mar. 2024.

[4] J. Y. Lu, and Y. Q. Liu, "Review on Linear Motor for Electromagnetic Launch and Its Control Technology," *Transactions of China Electrotechnical Society*, vol. 39, no. 19, pp. 5899–5913, Oct. 2024.

[5] J. H. Zhang, F. Q. Gao, and Z. X. Li *et al*., "Feedforward-based Variable Frequency Second Harmonic Current Suppression Strategy for Cascaded H-bridge Energy Storage Converter," *IEEE Transactions on Industrial Electronics*, vol. 73, no. 6, pp. 8405–8416, Jun. 2026.

[6] F. Xu, L. M. Shi, and Z. X. Li *et al*., "A Nonlinear Decoupled Modeling Method of Linear Induction Motor Propulsion System with Segmented Stator," *Transactions of China Electrotechnical Society*, vol. 40, no. 4, pp. 1023–1033, Feb. 2025.

[7] B. M. Perreault, "Optimizing Operation of switched Stator Linear Synchronous Motors," *Proceedings of the IEEE*, vol. 97, no. 11, pp. 1777–1785, Nov. 2009.

[8] Y. R. Wang, L. M. Shi, and F. Xu, "A Fast Subblock Switch Strategy for Segmented Long Primary Linear Machines based on an Asymmetric Parallel Topology," *IEEE Transactions on Industrial Electronics*, vol. 72, no. 3, pp. 2380–2391, Mar. 2025.

[9] R. B. Sepe, "Block Switching Transient Minimization for Linear Motors and Inductive Loads," U. S. Patent 20080284360, May 14, 2008.

[10] M. Y. Zhang, W. M. Ma, and X. H. Xu *et al*., "A Block Feeding Strategy for Linear Motor Considering Switching at Current-crossing Point," *Journal of Naval University of Engineering*, vol. 31, no. 4, pp. 11–16, 2019.

[11] M. Z. Ma, W. M. Ma, and H. L. Fan *et al*., "Switch Transient Process of Section Powered Long-primary Linear Induction Motor," *Electric Machines and Control*, vol. 19, no. 9, pp. 1–7, Dec. 2015.

[12] J. H. Liu, L. M. Shi, and K. Y. Guo *et al*., "A Switch Method to Suppress the Current Fluctuation for Segmented Powered Linear Motor," *Proceedings of the CSEE*, vol. 44, no. 4, pp. 1576–1586, Feb. 2024.

[13] C. T. Deng, F. Xu, and C. Zhao *et al*., "Switching Current Impact Reduction Method for Segmented Power Supply Linear Motor," in *Proc. of IECON 2022 – 48th Annual Conference of the IEEE Industrial Electronics Society*, Brussels, Belgium, Oct. 2022, pp. 1–6.

[14] C. T. Deng, F. Xu, and Z. X. Li *et al*., "A Suppresing Impact Current Method with Symmetrical Switching for Segmented Linear Motor," in *Proc. of 2023 14th International Symposium on Linear Drivers for Industry Applications*, Hannover, Germany, Jun. 2023, pp. 1–4.

[15] Y. F. Li, Z. X. Li, and C. Zhao *et al*., "Current Characteristics and Overcurrent Suppression in Segmented Power Switching Process of Long Primary Dual Three-phase Linear Motors," in *Proc. of ACCES 2024 – the 18th Annual Conference of China Electrotechnical Society*, Singapore, Sept. 2024, pp. 740–755.

[16] Y. F. Li, Z. X. Li, and C. Zhao *et al*., "A Novel Segment Switching Method for Dual Three-phase Linear Motors with Stator Segmented Powered," in *Proc. of 2024 27th International Conference on Electrical Machines and Systems*, Fukuoka, Japan, Nov. 2024, pp. 3431–3435.

[17] M. N. Ma, L. Y. Li, and J. P. Zhang *et al*., "Investigation of Cross-coupling Inductances for Long-stator PM Linear Motor Arranged in Multiple Segments," *IEEE Transactions on Magnetics*, vol. 51, no. 11, pp. 1–4, Nov. 2015.

[18] K. Y. Guo, Y. H. Li, and L. M. Shi *et al*., "A Phase-domain Model of Dual Three-phase Segmented Powered Linear PMSM for Hardware-assisted Real-time Simulation," *IEEE Transactions on Industry Applications*, vol. 58, no. 4, pp. 4511–4521, Jul.-Aug. 2022.

[19] S. J. Mu, J. Y. Chai, and X. D. Sun *et al*., "Analysis and Restrain of Mutual Inductance Asymmetry in the Sectionally Powered AC Linear Motor," *Transactions of China Electrotechnical Society*, vol. 30, no. 1, pp. 81–88, Jan. 2015.

[20] J. Xu, W. M. Ma, and J. Y. Lu *et al*., "Analysis of Air-gap Magnetic Field Distribution and Mutual Inductance Asymmetry of Sectionally Powered Linear Induction Motor," *Proceedings of the CSEE*, vol. 31, no. 15, pp. 61–68, May 2011.

[21] Y. F. Li, Z. X. Li, and H. Zhang *et al*., "Characteristics of Inductance Parameters in Single-layer Double-row Linear Induction Motors with Gramme-ring Windings Under Anti-phase Power Supply," *Transactions of China Electrotechnical Society*, vol. 40, no. 22, pp. 7140–7152, Nov. 2025.

[22] Y. F. Zhao, and T. A. Lipo, "Space Vector PWM Control of Dual Three-phase Induction Machine Using Vector Space Decomposition," *IEEE Transactions on Industry Applications*, vol. 31, no. 5, pp. 1100–1109, Sept.-Oct. 1995.

[23] M. Athans, and P. L. Falb, *Optimal Control: an Introduction to the Theory and its Applications*. Courier Corporation, 2013, pp. 376–377.

[24] J. W. Chui, and S. K. Sui, "New Current Control Concept-minimum Time Current Control in the Three-phase PWM Converter," *IEEE Transactions on Power Electronics*, vol. 12, no. 1, pp. 124–131, Jan. 1997.

[25] M. Y. Zhang, and L. M. Shi, "Modeling and Cooperative Control of Segmented Long Primary Double-sided Linear Induction Motor," *IEEE Transactions on Industrial Electronics*, vol. 70, no. 2, pp. 1706–1716, Feb. 2023.

[26] Y. S. Hu, Z. Q. Zhu, and K. Liu, "Current Control for Dual Three-phase Permanent Magnet Synchronous Motors Accounting for Current Unbalance and Harmonics," *IEEE Journal of Emerging and Selected Topics in Power Electronics*, vol. 2, no. 2, pp. 272–284, Jun. 2014.

[27] H. S. Che, E. Levi, and M. Jones *et al*., "Current Control Methods for an Asymmetrical Six-phase Induction Motor Drive," *IEEE Transactions on Power Electronics*, vol. 29, no. 1, pp. 407–417, Jan. 2014.

Yanfei Li received the B.Eng. degree in electrical engineering and its automation from the Northeast Electric Power University, Jilin, China, in 2018 and the M.S. degree in high voltage and insulation technology from the University of Chinese Academy of Sciences (UCAS), Beijing, China in 2021. He is currently pursuing a Ph.D. degree in power electronics and power drives at UCAS. His research focuses on modeling and control of linear motors for high-speed electromagnetic propulsion systems.

Zixin Li received the B.Eng. degree in industry automation from the North China University of Technology, Beijing, China, in 2005, and the Ph.D. degree in power electronics and power drives from the Institute of Electrical Engineering, Chinese Academy of Sciences, Beijing, China, in 2010.

Since 2010, he has been with the Institute of Electrical Engineering, Chinese Academy of Sciences, where he is currently a Professor and Deputy Director. He has authored or coauthored more than one hundred academic papers and holds more than twenty invention patents in China. His research interests include power electronics and electromagnetic drive technologies and their applications in power grids, transportation, energy, and other fields.

Dr. Li is currently serving, or has previously served, as an Associate Editor for *IEEE Transactions on Power Electronics*, *IET High Voltage*, *Journal of Power Electronics*, and *Chinese Journal of Electrical Engineering*. He was the recipient of the IEEE Power Electronics Society Richard M. Bass Outstanding Young Power Electronics Engineer Award of 2015 for his contributions to multilevel and HVDC converters. He was elected as a Fellow of the Institution of Engineering and Technology (IET) in 2019.

Hang Zhang received the Ph.D. degree in power electronics and power drives from the Institute of Electrical Engineering, Chinese Academy of Sciences, Beijing, China, in 2020.

Since 2020, he has been with the Institute of Electrical Engineering, Chinese Academy of Sciences, Beijing, China, where he is currently a Senior Engineer. His research interests include circuit topology, analysis, and control of high-power electronic converters, especially their applications in high- or medium-voltage direct current fields.

Fei Xu (Member, IEEE) received the B.S. and M.S. degrees from Central South University, Changsha, China, in 2006 and 2009, respectively, and the Ph.D. degree in power electronics and power drives from the Institute of Electrical Engineering, Chinese Academy of Sciences, Beijing, China, in 2012.

He is an Associate Professor with the Institute of Electrical Engineering, Chinese Academy of Sciences, Beijing, China, where he has worked since 2013. His research interests include model and control of high-speed linear motors and high-power electronics.

Cong Zhao received the B.Eng. degree in electrical engineering from Tsinghua University, Beijing, China, in 2012, and the Ph.D. degree in power electronics and power drives from the Institute of Electrical Engineering, Chinese Academy of Sciences, Beijing, China, in 2017.

Since 2017, he has been with the Institute of Electrical Engineering, Chinese Academy of Sciences, Beijing, China, where he is currently an Associate Professor. His research interests include topology, analysis, and control of modular multilevel converters and power electronic transformers.

Fanqiang Gao received the B.Eng. degree in automation control from the Huazhong University of Science and Technology, Wuhan, China, in 2006, and the Ph.D. degree in power electronics and power drives from the Institute of Electrical Engineering, Chinese Academy of Sciences, Beijing, China, in 2012.

In 2012, he joined the Institute of Electrical Engineering, Chinese Academy of Sciences, where he is currently an Associate Professor. His research interests include the analysis and control of power electronic converters in high-power fields.

Yaohua Li received the Ph.D. degree in power electronics and power drives from the Tsinghua University, Beijing, China, in 1994.

From 1995 to 1997, he was a Postdoctoral Research Fellow with the Institute of Electrical Machine, Technical University of Berlin, Germany. In 1997, he joined the Institute of Electrical Engineering, Chinese Academy of Sciences, Beijing, China, and is currently a Professor and Director. His research fields include analysis and control of electrical machines and power electronics.